AIAA JOURNAL
Vol. 56, No. 11, November 2018

Acoustic Prediction of LAGOON Landing Gear: Cavity Noise and Coherent Structures

Tulio R. Ricciardi* and William R. Wolf†
University of Campinas, 13083-860 Campinas, Sao Paulo, Brazil
and
Rachelle Speth‡
The Boeing Company, St. Louis, Missouri 63134

DOI: 10.2514/1.J056957

Detached-eddy simulations of the LAGOON landing gear configuration are performed using different unstructured meshes. One mesh is generated based on available experimental and numerical data, and based on this first mesh, a second one is carefully designed to improve the solutions in regions of strong unsteadiness. Results are presented in terms of steady and unsteady hydrodynamic data as well as noise predictions, which are performed using the Ffowcs-Williams and Hawkings formulation. Numerical results show good agreement with experimental data available in the literature. A wavelet transform analysis demonstrates that the sound generation in the cavity is an intermittent process that leads to strongly varying amplitudes of the surface pressure and the far-field noise radiation. A proper orthogonal decomposition is employed to identify coherent energetic structures responsible for the cavity tones. Finally, it is shown how the local flow topology affects the impingement of these coherent structures on the cavity.

Nomenclature

A	=	proper orthogonal decomposition (POD) left singular matrix
C	=	POD correlation matrix
Ng	=	number of grid points
Nf	=	filter function half-width
Nt	=	number of snapshots
t	=	time, s
$\boldsymbol{U}$	=	instantaneous velocity field, m/s
u', v', w'	=	x, y, and z Cartesian components of velocity fluctuation, m/s
V	=	cell volume, m^3
$\boldsymbol{X}$	=	Cartesian components, m
λ	=	POD singular value
Φ	=	POD matrix of spatial coefficients

I. Introduction

EFFORTS toward aircraft noise reduction are of paramount importance since regulations have become increasingly stringent to limit noise levels generated by aircraft. Airframe noise associated with the unsteady turbulent flow around the aircraft has become a significant source of noise, especially during approach conditions in which landing gears, slats, and flap side edges are important noise sources [1]. Aerodynamic noise from landing gears is broadband in nature with distinct narrowband peaks due to coherent turbulent structures associated with extended small components of different sizes [2,3]. The broadband noise is generated by turbulent flow separation along the blunt elements and the subsequent interaction of the generated turbulent wakes with other elements [1]. The presence of holes and cavities in the landing gear may introduce additional noise sources including narrowband peaks due to cavity resonance modes [4].

Besides the prediction of individual airframe noise sources, wake interactions lead to increased complexity since a simple summation of the noise sources from landing gears and deployed high lift devices would not be representative of the actual airframe noise prediction. In this case, one should also consider the installation effects of landing gear noise on wings, the fuselage, landing gear doors, flaps, and engines. Important physical mechanisms such as reflection and diffraction of acoustic waves and turbulent wake interaction may occur along these solid surfaces. For example, the turbulent wake of the landing gear may impinge directly in the flap system, resulting in an even more complicated noise source [5,6]. Furthermore, changes in the velocity field under the wing and fuselage modify the incident flow in the gear [7].

Despite all the aforementioned complications, studying the separate airframe noise components, i.e., nose and main landing gears, as well as slats and flaps, is a necessary task to develop a complete understanding of the overall airframe noise problem. This approach is still required for the improvement of more robust predictive methods of aircraft noise. Recently, several groups have studied the LAGOON nose landing gear configuration in different categories of the AIAA Benchmark problems for Airframe Noise Computations (BANC) workshop [8–16]. This model consists of a simplified 2:5 scaled nose landing gear composed of wheels, cavities, an axle, and a strut. Casalino et al. [13,17], Giret [18], and de la Puente et al. [19] presented an analysis of tonal noise from cavity resonance modes present in the LAGOON configuration. It is important to mention that cavity resonances may also be excited in realistic landing gear configurations [20].

This Paper presents flow simulations and acoustic predictions of the LAGOON landing gear. We perform detached-eddy simulations (DES) using the Boeing-CFD code (BCFD). For the acoustic predictions, the Ffowcs-Williams and Hawkings (FWH) analogy [21] is employed, considering flow effects and also a quiescent medium. Results from the current numerical simulations are compared against an available experimental database provided by ONERA [22,23], and good agreement is shown in terms of steady and unsteady data for different mesh configurations. One mesh is generated based on available experimental and numerical data, and based on this first mesh, a second one is carefully designed to improve the solutions in regions of strong unsteadiness. For the second mesh, we also analyze the effects of

Presented as Paper 2017-3010 at the 23rd AIAA/CEAS Aeroacoustics, Denver, CO, 5–9 June 2017; received 9 December 2017; revision received 3 May 2018; accepted for publication 24 June 2018; published online 28 September 2018.

*Ph.D. Student, Department of Energy, School of Mechanical Engineering.
†Assistant Professor, Department of Energy, School of Mechanical Engineering. Member AIAA.
‡CFD-CAA Engineer, Boeing Research and Technology.

the time step on the statistics of surface pressure spectra. Here, we apply a wavelet transform and proper orthogonal decomposition to study the cavity noise sources. The former technique is employed to verify the intermittency of noise generation, and the latter is used to identify coherent energetic structures that may excite cavity resonance modes. Different POD techniques are tested for the previous task, and we apply a filter function to the POD correlation matrix, allowing the analysis of spatial modes at specific frequencies [24].

II. Simulation Setup

The setup of the current simulation is briefly described in the following sections. The flow configuration is the same as in the experiments; hence, the Mach number is set as 0.23, and the freestream temperature, velocity, and density are, respectively, 293 K, 99447.7 Pa, and 1.18 kg/m^3. The perfect gas equation relates pressure to density and temperature, while the viscosity is evaluated using Sutherland's law. The Reynolds number is 1.54×10^6 based on the wheel diameter of 0.3 m.

A. Numerical Methodology

The Navier–Stokes equations are solved using the BCFD [25,26], with a hybrid methodology that includes the Reynolds-averaged Navier–Stokes (RANS) solution and large-eddy simulation with a modification for delayed transition between the methods [27,28]. The DES coefficient is set as 0.65, and the turbulence model in the RANS region is the Spalart–Allmaras [29].

For the time marching scheme, an implicit dual time step method is employed together with the optimized second-order backward differencing formulation (BDF2OPT) proposed by Vatsa et al. [30]. The BDF2OPT represents a stable blend between a second- and a third-order backward differencing scheme, and together with the dual time stepping scheme, they allow for large time steps with both stability and accuracy. Here, the dual time stepping method solves for 15 cycles in pseudotime using a line implicit Gauss–Seidel algorithm before advancing the solution one physical time step. Here, to assess the dependence of the solutions on the time step, we employed $\Delta t = 7.5$ and 10 μs. Depending on the grid cell, the residual in the pseudotime may reduce from one to four orders in the current calculations.

The inviscid flux term appearing in the Navier–Stokes equations is computed using a second-order-accurate HLLE scheme with a bounded central differencing approach for reduced numerical dissipation of the flux reconstruction [31]. The gradient calculation is performed using a least-square method based on cell center values. Also, the Barth and Jespersen [32] flux limiter is employed. For the viscous terms, a full discretization of the Navier–Stokes equations is performed using the face-tangent method.

B. Description of Surface Grids

The surface grid is of paramount importance for acoustic predictions since the propagation methodology employed in the present work is the FWH method [21]. If the FWH formulation is solved for a solid surface, the only input from the numerical simulations would be the unsteady pressure along the surface, requiring good accuracy of this parameter. In this work, we employ an unstructured grid due to its flexibility, which allows good control over the mesh refinement in specific regions of the flow. The Boeing-NPARC proprietary software MADCAP is used to generate the surface grids, and here, only triangular elements are employed along the solid surfaces.

Simulations are performed using different meshes, and the first surface mesh was designed with a refinement on regions where pressure fluctuations are more significant, based on experimental data from the LAGOON geometry [22,23]. Hence, the axle and cavities have finer elements, while the base of the strut and wheel has coarser elements. Also, for all components of the landing gear, the regions where flow separation occurs are more refined due to the higher unsteadiness. The upper portion of the strut is deliberately coarsened since, based on the literature, this component is not a main source of noise in the LAGOON. This consideration leads to a reduction in the overall number of mesh elements without losing accuracy on the far-field noise predictions.

After an initial assessment of the surface pressure, both in terms of steady and unsteady data, a second mesh was designed to locally improve results compared to those obtained for the first mesh.

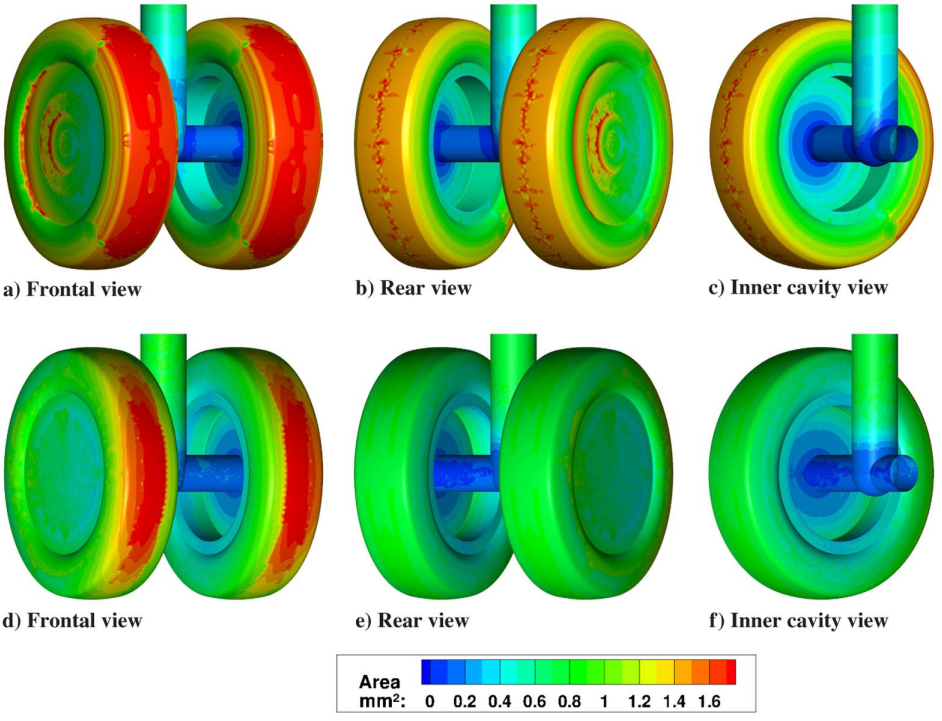

Fig. 1 Area of the surface elements. Top and bottom rows show meshes 1 and 2, respectively.

Table 1 Number of surface elements on the landing gear components

Component	Mesh 1	Mesh 2	Variation, %
Axle	212,054	170,446	−19.62
Cavity	211,952	200,988	−5.17
Strut	185,112	131,054	−29.20
Wheel	342,924	499,632	+45.70
Total	952,042	1,002,120	+5.26

The main differences between the meshes are the overall refinement increase along the wheels (with special attention to corners); the external shallow cavities of the wheels; and, more importantly, the edges of the internal cavities of the wheels. For the second mesh, the elements of the wheels are more comparable in size with respect to those in the axle and cavity. The second mesh also has a more gentle stretching in the boundary layer regions, which leads to a reduced numerical dissipation. The stretching ratio in the axle–strut junction is also reduced, leading to a smoother grid in that region. These modifications are shown in Fig. 1, for the first and second mesh configurations. In this figure, it is important to notice that the blue regions indicate finer elements than those colored in red.

To avoid an excessive increase in the number of surface elements, regions that have been well resolved in the first simulation, i.e., the inner region of the cavity and the axle, are slightly coarsened for the second simulation. Still, regarding the axle, the grid stretching in the transverse direction is smoother in the second mesh configuration in such a way that the axle span is more uniformly refined (see Figs. 1c and 1f). In this sense, the first mesh has a concentration of elements in the junctions with the cavity and strut. Hence, the first surface mesh has approximately 950,000 triangular elements, while the second one has 1,000,000 (an increase of 5% in the number of elements). Table 1 indicates the changes in the number of surface elements along the landing gear components for both mesh configurations.

C. Description of Volume Grids

In this work, we use the AFLR software developed by University of Mississippi for the volume mesh generation [33]. The modifications in the surface mesh, presented in Sec. II.B, directly impact the volume grids presented in Fig. 2. The first figure shows the volumes of the cell elements for the first mesh, considered here as the baseline case, and the second figure presents the volume sizes for the second mesh configuration, considered here as the improved case. Refined regions at the surface lead to finer discretizations of the volume mesh, reducing the numerical dissipation and increasing accuracy. To avoid an excessive count of elements, the extent of the refined region in the wake of the wheels is reduced for the second mesh configuration. The refined triangular region behind the landing gear, shown for the $y = 0.0$ plane in Fig. 2c, is modified to a circular refined region around the wheels as presented in Fig. 2f. With these modifications, the overall number of volume elements in the first and second mesh configurations is 92,000,000 and 99,000,000, respectively.

One can observe in Fig. 2 that the second mesh has smaller cell elements just upstream of the inner cavities, inside the wheels, and also along the wake of the axle, toward the back portion of the wheels. It is possible to see that the external cavities of the wheels also have more refined elements for the second mesh. These features lead to a better capture of the unsteady physical mechanisms responsible for noise generation in these regions.

For both mesh configurations, the height of the first prismatic elements normal to the wall is imposed as 7.5 μm. This value is close to the values used in the simulations of the LAGOON performed by other groups [15]. Figure 3 shows a detailed view of the volume mesh around the rear portion of the wheel for both baseline and improved grids. This figure highlights the grid along the boundary layer, which is composed of around 35 prismatic elements normal to the wall, before transitioning to the tetrahedral elements. One can clearly see that the improved grid is more refined in the internal cavity as well as on the external shallow cavity and downstream of the wheel.

III. Numerical Results

This section presents results for one simulation performed using the baseline grid and two simulations obtained using the improved grid. For the improved grid, two different time steps are employed, $\Delta t = 7.5$ and 10 μs, while for the first grid, only the larger time step is used. Numerical results are presented in terms of steady and unsteady hydrodynamic data, which include mean and rms velocity profiles measured along lines in the wake region as well as

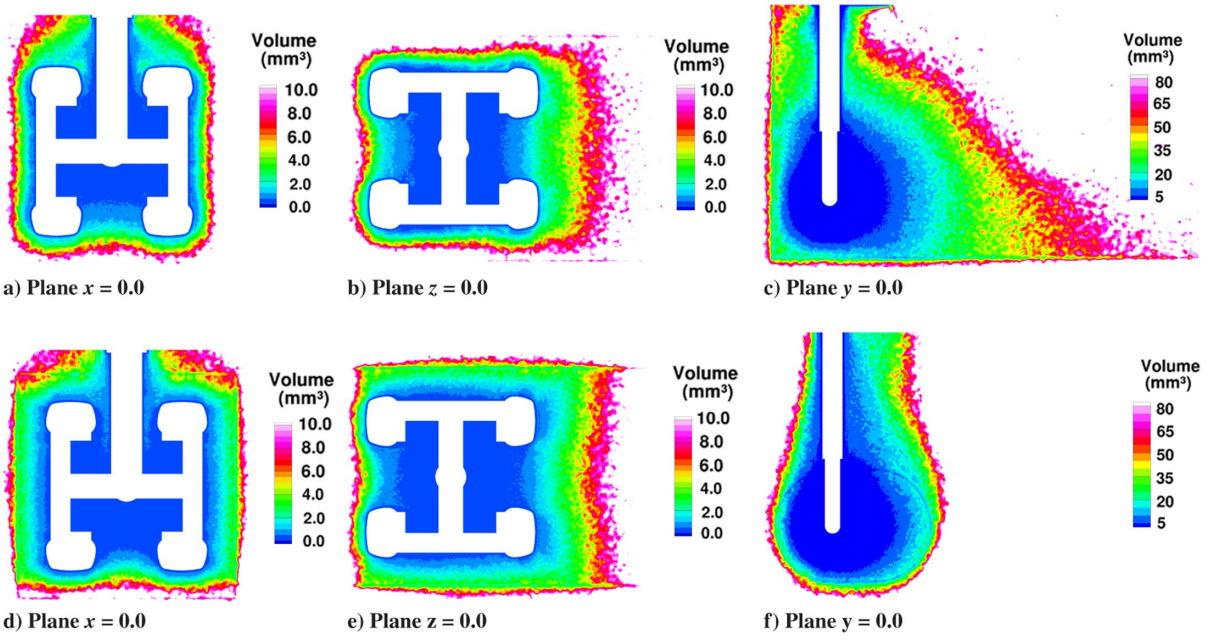

Fig. 2 Volume of cell elements around the solid surface. Top and bottom rows show meshes 1 and 2, respectively.

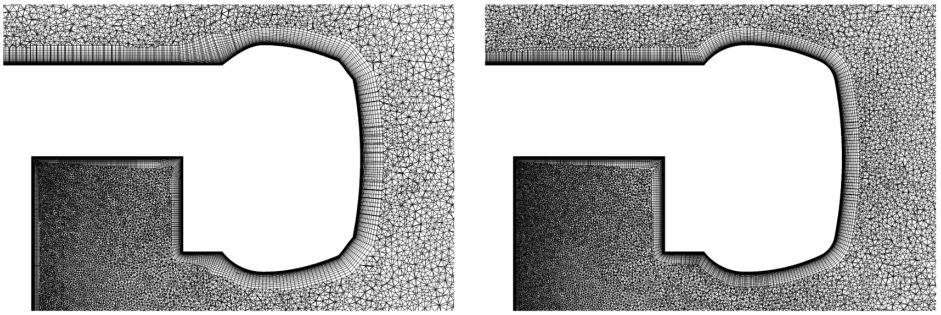

a) Baseline mesh b) Improved mesh

Fig. 3 Detail of the boundary layer mesh along the wheel.

surface pressure coefficient and spectra of pressure fluctuations. The FWH acoustic analogy is employed using a solid surface to compute the far-field noise. Therefore, the unsteady surface pressure is the only quantity used for the acoustic predictions. Finally, proper orthogonal decomposition of the flowfield is used to identify coherent structures responsible for the tonal noise generation at 1.5 kHz.

For the baseline mesh, results are presented for a reduced period in order to quickly assess the numerical results. Therefore, 6144 snapshots are employed for the computation of the flow statistics including mean quantities along the wake as well as pressure measurements on the surface. For the improved mesh, results are presented for 20,480 snapshots for $\Delta t = 10$ μs. This represents a total period of 0.2048 s, which gives approximately 53 flow-through times based on the wheel diameter. After that, the time step is reduced to $\Delta t = 7.5$ μs to assess the influence of this parameter in the computation of surface pressure spectra. For this study, 8192 snapshots are employed in the calculations.

A. Surface Data

First, we provide a qualitative analysis of the mean and rms pressure values along the landing gear surface for both meshes. These results are shown in Figs. 4 and 5 for mean and rms pressure values. No significant differences can be observed between the results obtained by the two meshes.

To assess the quality of the numerical solutions, the mean and unsteady pressure values are evaluated at the same locations as in the BANC experiment, i.e., for 64 static plus 27 Kulite sensors, as depicted in Fig. 6.

Mean values of surface pressure are presented in Fig. 7 in the form of the nondimensional pressure coefficient Cp. It is worth emphasizing that the simulation employs an open domain,

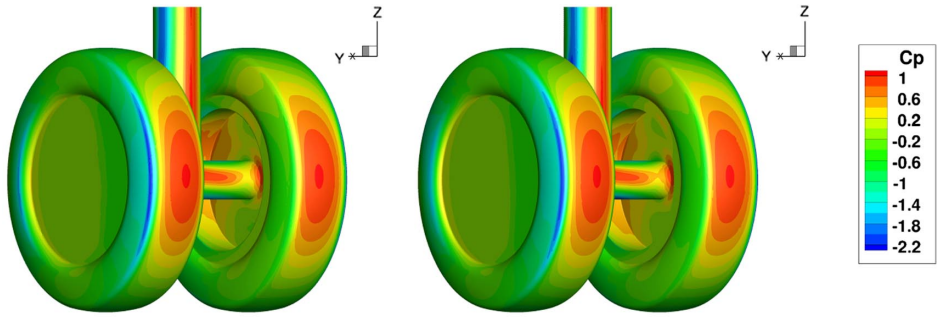

a) Baseline grid b) Improved grid

Fig. 4 Results in terms of mean pressure along the surface of the landing gear.

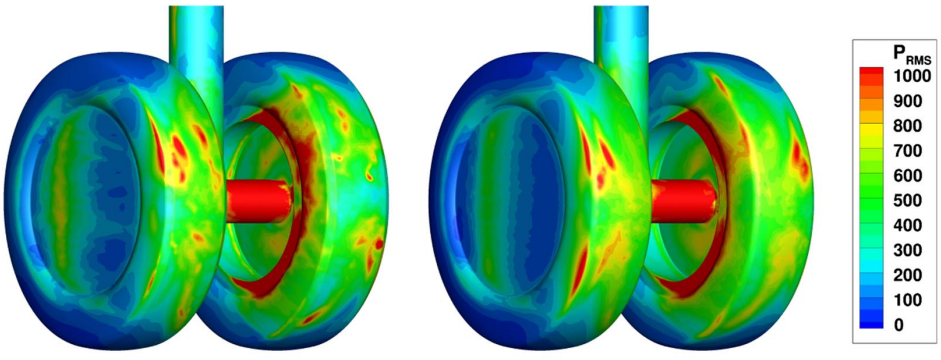

a) Baseline grid b) Improved grid

Fig. 5 Results in terms of rms pressure along the surface of the landing gear.

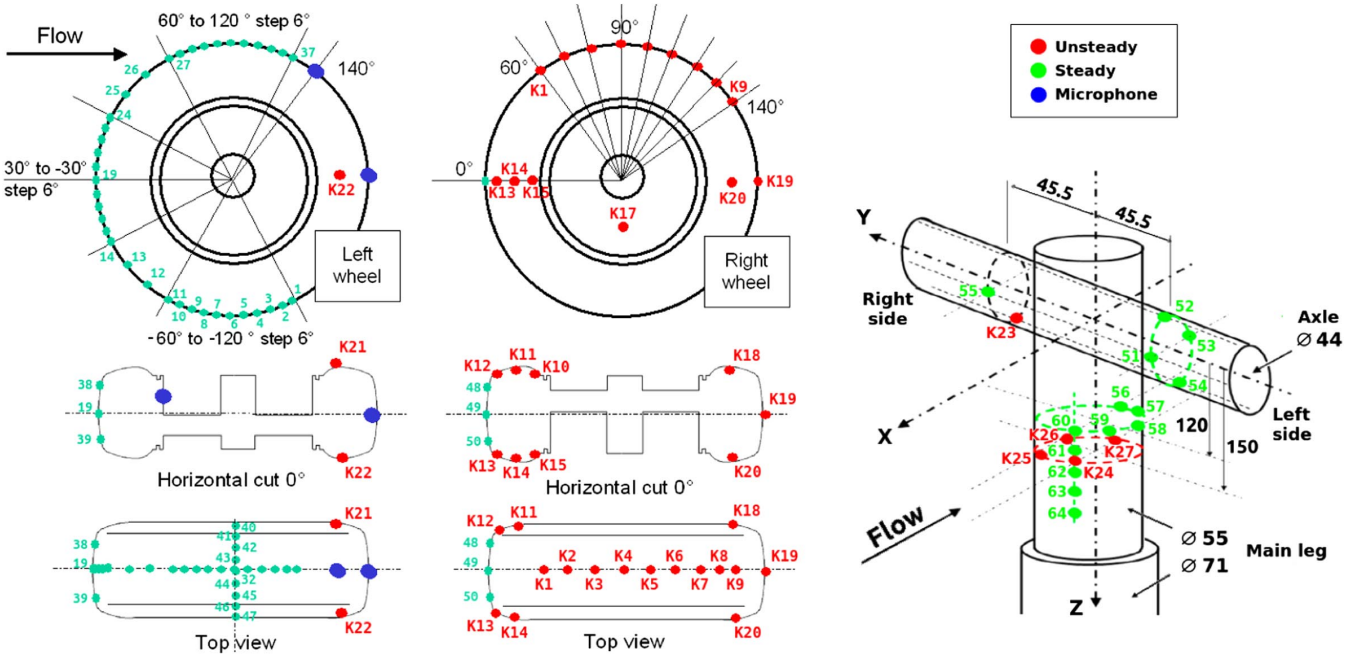

Fig. 6 Surface pressure probe locations extracted from [22,23].

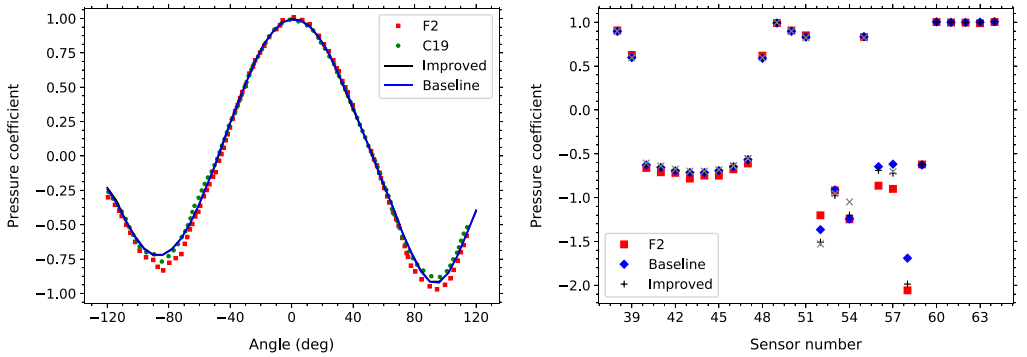

a) Pressure along the wheel perimeter **b) Pressure for other locations shown in Fig. 6**

Fig. 7 Comparison of pressure coefficient *Cp* among numerical simulations and experiments.

while experimental results are obtained at ONERA's F2 closed wind tunnels. Hence, the blockage effect in the presence of the geometry forces the fluid to accelerate, and some discrepancies are expected mainly for negative pressure coefficients.

The results of the mean pressure on the wheel perimeter (static sensors 1 to 37) are compared to the wind tunnel measurements in Fig. 7a. It is possible to see that numerical results have a better comparison to the open jet wind tunnel, C19, as expected. Also, no significant difference in terms of mean pressure is observed for the simulations with the baseline and improved grids. Figure 7b shows the measurements at other points along the landing gear surface. Static sensors 38 to 50 are also placed on the wheel, and results agree reasonably well with the experiments. Again, both meshes provide similar results. In Fig. 7b, the black and gray cross symbols represent results obtained for different wheels for the improved mesh. Sensors 52 to 54 and 56 to 58 present slight differences between the solutions from the numerical simulations. In the first simulation with the baseline grid, the flow along the axle (sensors 51 to 55) is better resolved due to the improved refinement on the region where the sensors are placed. On the other hand, for the second simulation, the results along the strut (sensors 56 to 64) show better agreement with the experiments.

Numerical and experimental results are compared in terms of unsteady pressure fluctuations in Figs. 8–13. The surface pressure along the LAGOON geometry is analyzed using a temporal signal stored with a frequency sampling of 100 kHz. In these figures, the values in the y axis represent the power spectral density (PSD) of the surface pressure fluctuations. The blue line represents the results from the baseline simulation obtained using mesh configuration 1, while the black line represents the results for the improved simulation computed using mesh 2, called *Imp 1* in the legends. To check for asymmetries in the numerical solutions, results for mirrored positions along the landing gear are presented for the improved simulation in gray lines. In the experiments, a similar study is also performed, and Kulite sensors 18 and 20 are symmetric with respect to 22 and 21, respectively. The yellow line in the figures represents the numerical results obtained using mesh 2 and the reduced time step, here called *Imp 2* in the legends. As stated by ONERA in the technical reports discussing the experimental data, sensors K12 and K16 present strange behavior in the experiments, and hence, they are not used in the comparisons, as well as Kulite K3 in the F2 wind tunnel experiment.

For both simulations, the signal processing is performed using a fast Fourier transform of the data together with the Tukey window

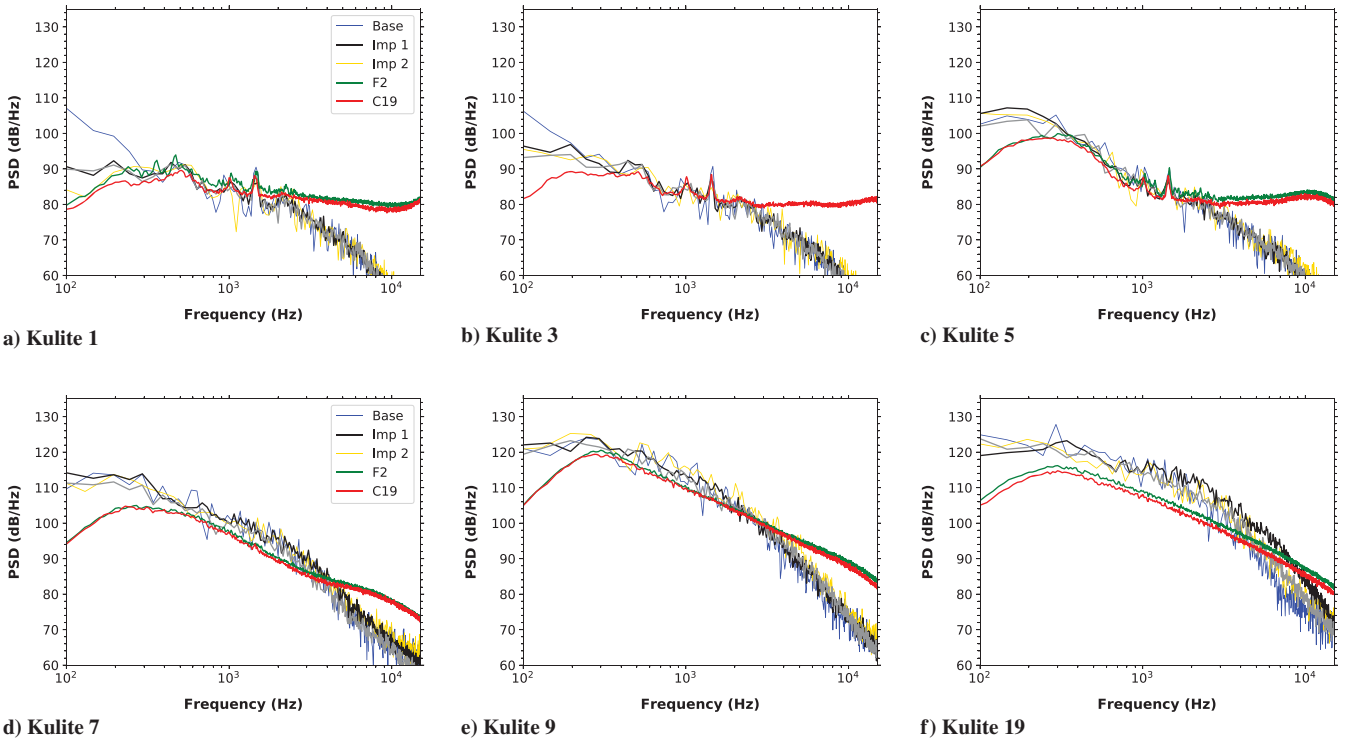

a) Kulite 1 b) Kulite 3 c) Kulite 5

d) Kulite 7 e) Kulite 9 f) Kulite 19

Fig. 8 Power spectral density of surface pressure for sensors positioned in the perimeter of the wheel.

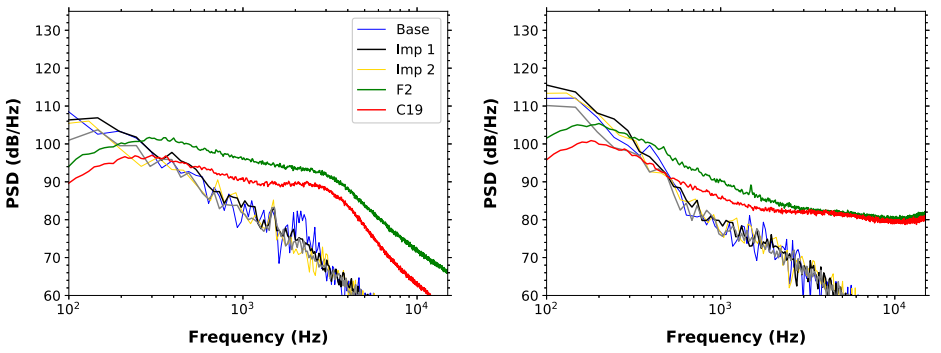

a) Kulite 10 b) Kulite 11

Fig. 9 Power spectral density of surface pressure for sensors located outside of the wheel in the upstream region.

function with $\alpha = 0.25$. The signals have 2048 samples, resulting in a frequency interval of 48.8 Hz for the individual bins. The overlapping among bins is 50%, and the average of the PSD from the bins is used to smooth out the spectra. For the baseline grid, the total number of measurements is 6144 (resulting in 5 bins), and for the improved grid, a total of 20,480 measurements (19 bins) are employed in the statistics. For the simulations performed with the reduced time step, 8192 measurements are employed in the statistics, considering a frequency interval of 36.6 Hz for the individual bins. In this case, the signals also have 2048 samples, resulting in seven bins.

The results obtained for the sensors in the perimeter of the wheel are presented in Fig. 8, in which one can see a lower cutoff frequency compared to the experiments for sensors K1 to K5. This behavior is assumed to be due to the tripping in the experiment, which is not fully reproduced in the numerical simulations. Also, the boundary layer in a DES simulation is solved by a RANS procedure that is not able to solve small scales of turbulence and their associated high-frequency pressure fluctuations. Downstream of the wheel, turbulence fluctuations are more intense such that the PSD levels from probes K1, K3, and K5 (located upstream) are considerably lower than those from probes K7, K9, and K19 (located downstream). In fact, the former probes are located in regions where the boundary layers may not be fully turbulent. Along the turbulent region, where the PSD levels are higher, it is not possible to visualize any sharp tones due to the higher amplitudes of the broadband spectra. Comparing the numerical results, the solutions obtained using the improved grid present a reduced attenuation of the high-frequency content of the spectra for Kulites K7, K9, and K19. However, for these sensors, the numerical solutions still overpredict the fluctuations in the low and moderate frequencies compared to the experimental data.

Sensors K10 to K15 are placed in the plane $z = 0.0$ m, in the quasi-steady region of the flow, upstream of the axle. Pressure spectra for these sensors are presented in Figs. 9 and 10. These probes are located along the internal and external sides of the wheel. The unsteady pressure spectra for the Kulites along the external portion of the wheel (K10 and K11 shown in Fig. 9) decay quickly and do not match the experiments, even for the improved grid. The experiments report data corruption in Kulite 12, and hence, a comparison for this sensor is not presented. The spectra from Kulites facing inward toward the wheel (K13, K14, and K15 shown in Fig. 10) present two

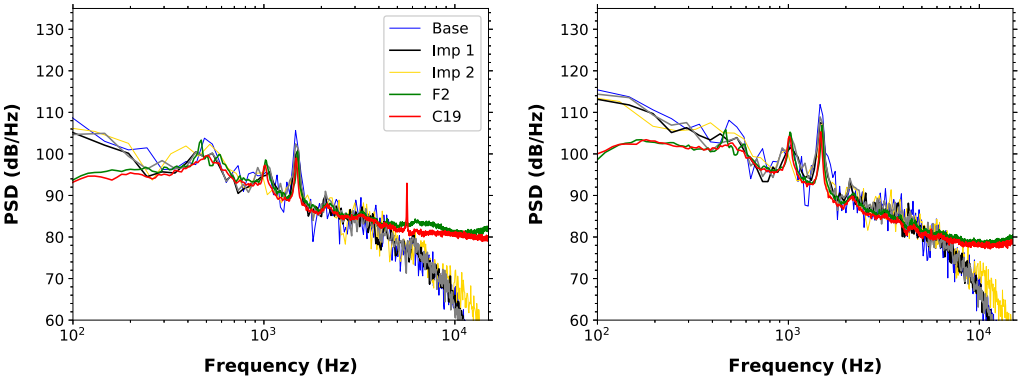

a) Kulite 13 b) Kulite 14

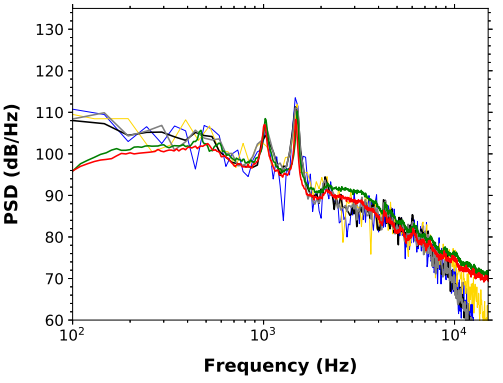

c) Kulite 15

Fig. 10 Power spectral density of surface pressure for sensors located inside the wheel in the upstream region.

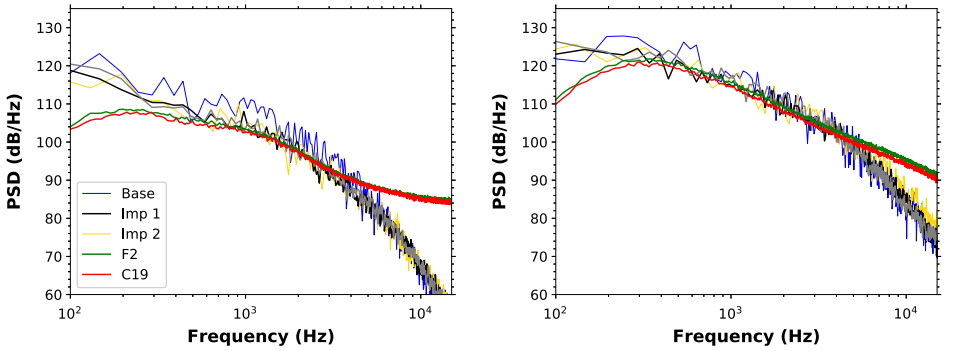

a) Kulite 18 (black) and 22 (gray) b) Kulite 20 (black) and 21 (gray)

Fig. 11 Power spectral density of surface pressure for sensors placed at the wheels in the downstream region.

tonal peaks at frequencies 1.0 and 1.5 kHz. These tones are observed for all numerical simulations. One can also see that the grid in the region of probe K15 is able to resolve the spectrum for frequencies close to 10.0 kHz.

The Kulites placed in the wake of the axle and cavity, in the plane $z = 0.0$ m, present higher values of the surface pressure PSD due to the turbulence levels in the wake. In Fig. 11a, it is worth noticing that sensor K18 is symmetric with respect to K22, both located in the outward side of the wheels. The results for the upstream Kulites K10 and K11 mismatch the experiment; however, the solution obtained for the downstream positions K18 and K22 show reasonable agreement with the experiment. On the other hand, results obtained for sensor K20 and its symmetric K21, both at the internal side of the wheels, match the experiments up to 4 kHz as shown in Fig. 11b.

Figure 12 shows results in terms of pressure fluctuations at the surface of the strut. As one can notice, the solutions obtained with the improved grid are able to capture the 1 kHz tonal noise peak observed in the experiments for K25. This tone is not present in the simulation performed using the baseline grid. Moreover, the results from the improved grid and the smaller time step present a better prediction for K27. Although the improved grid leads to better results in the strut, calculations still underpredict the PSD levels compared to the experiments since the strut is not as refined as the other components. Hence, smaller elements should be employed in this region for a better prediction of the pressure fluctuations, mainly close to the detachment point where rms values are higher, as shown in Figs. 4 and 5.

In Fig. 13a, results are shown for sensor K17, positioned in the bottom of the cavity. Although the cavity is slightly coarsened for mesh 2, the frequency cutoff is still around 8 kHz for both simulations. For sensor K23, placed on the surface of the axle, the numerical solution underpredicts the pressure fluctuations for a few

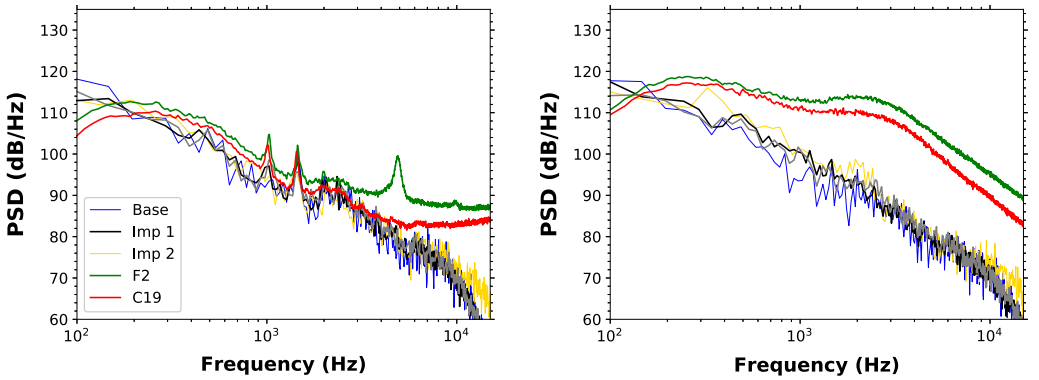

a) Kulite 25 b) Kulite 26

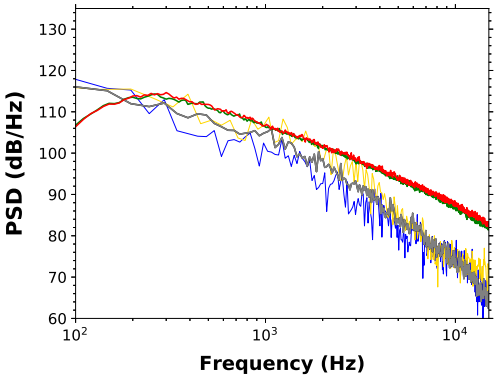

c) Kulite 27

Fig. 12 Power spectral density of surface pressure for sensors located in the strut.

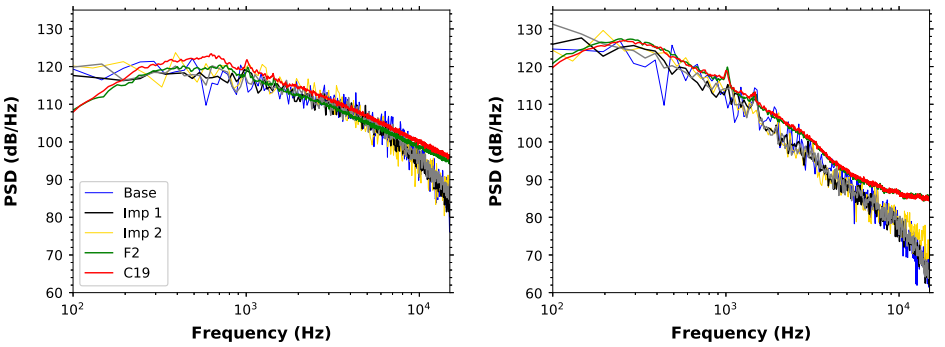

a)Kulite17 b) Kulite 23

Fig. 13 Power spectral density of surface pressure for sensors located in the axle and cavity.

decibels, but the overall shape of the curve has good agreement with the experiment, as shown in Fig. 13b. Even though the improved mesh is slightly coarser along the cavity and strut, its solution leads to results similar to those from the baseline mesh.

Summarizing, it is possible to see an improvement in the results obtained by the simulations performed using the improved grid, mainly in terms of the solution of the 1 kHz tonal noise peak. This tone was not clearly observed in the solution from the baseline grid. However, it is important to say that the treatment of the signals plays an important role in the resulting spectra, which may mask the tones. It is not clear if a longer signal for the first simulation would lead to improved results in terms of postprocessing. In terms of the time step, the only significant improvement due to the time-step reduction was observed for the low-to-middle frequency range of the spectrum for Kulite K27.

With the use of a wavelet transform, due to their compact support, it is possible to identify transient phenomena, differently from the Fourier transform that assumes signal periodicity. The continuous wavelet transform (CWT) decomposes the signal in terms of an specific event and its frequency [34]. Hence, it is possible to identify intermittent turbulent structures at specific frequencies. This way, the application of the CWT with the Morlet wavelet for the temporal signal of Kulite 15 and at the point symmetric to K15, both placed on the edge of the cavity, indicates that pressure fluctuations at 1.5 kHz are not periodic but, instead, are intermittent, as shown in Fig. 14. In this figure, it is possible to see large peaks for events with the frequencies of 1 and 1.5 kHz.

B. Wake Data

To check for a statistically converged flow, we include visualizations of the velocity fields in the wake in the plane $z = 0.0$ m. Figure 15 presents mean velocity fields obtained by particle image velocimetry (PIV) measurements from [22]. Results

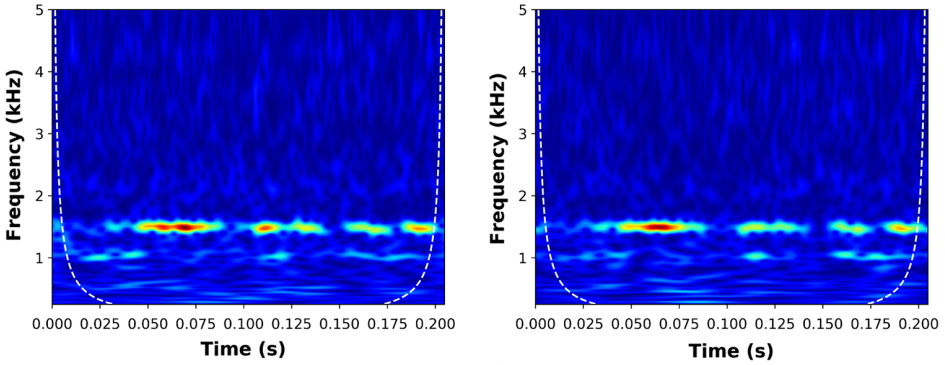

a) Kulite 15 b) Kulite 15 mirrored

Fig. 14 Wavelet transform of the pressure signal of Kulite 15, placed on the edge of the cavity.

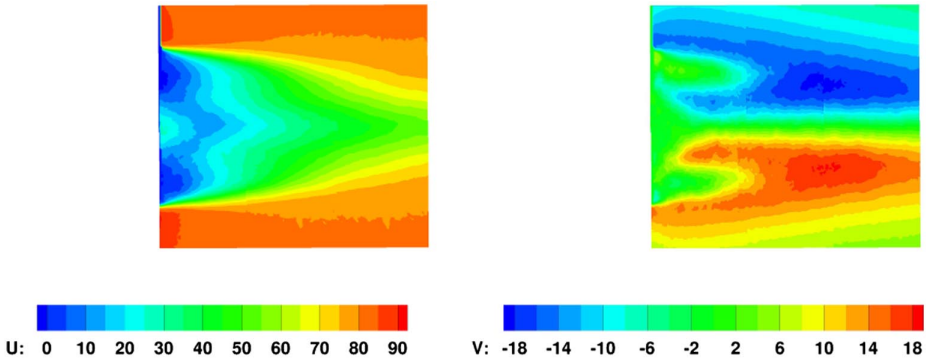

a) *U* component b) *V* component

Fig. 15 Mean velocity fields from PIV measurements.

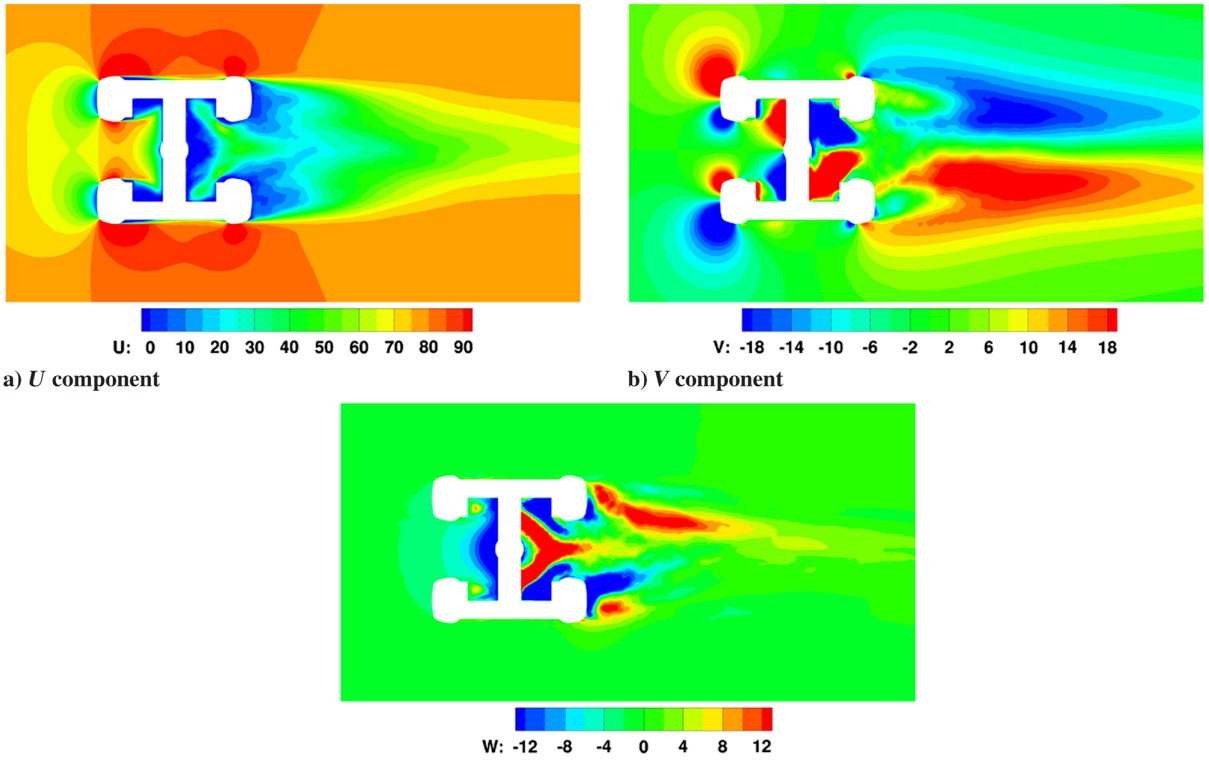

a) *U* component b) *V* component

c) *W* component

Fig. 16 Mean velocity contours of the three velocity components for the baseline grid.

shown in Figs. 16–19 present numerical results for the three components of velocity, in terms of mean and rms values, including the comparison of the two simulations performed with $\Delta t = 10\ \mu$s. The asymmetry of the w velocity component is considerably reduced in the simulation performed using the improved grid not only due to the better resolution behind the wheels but also because of the longer time period used to compute the statistics.

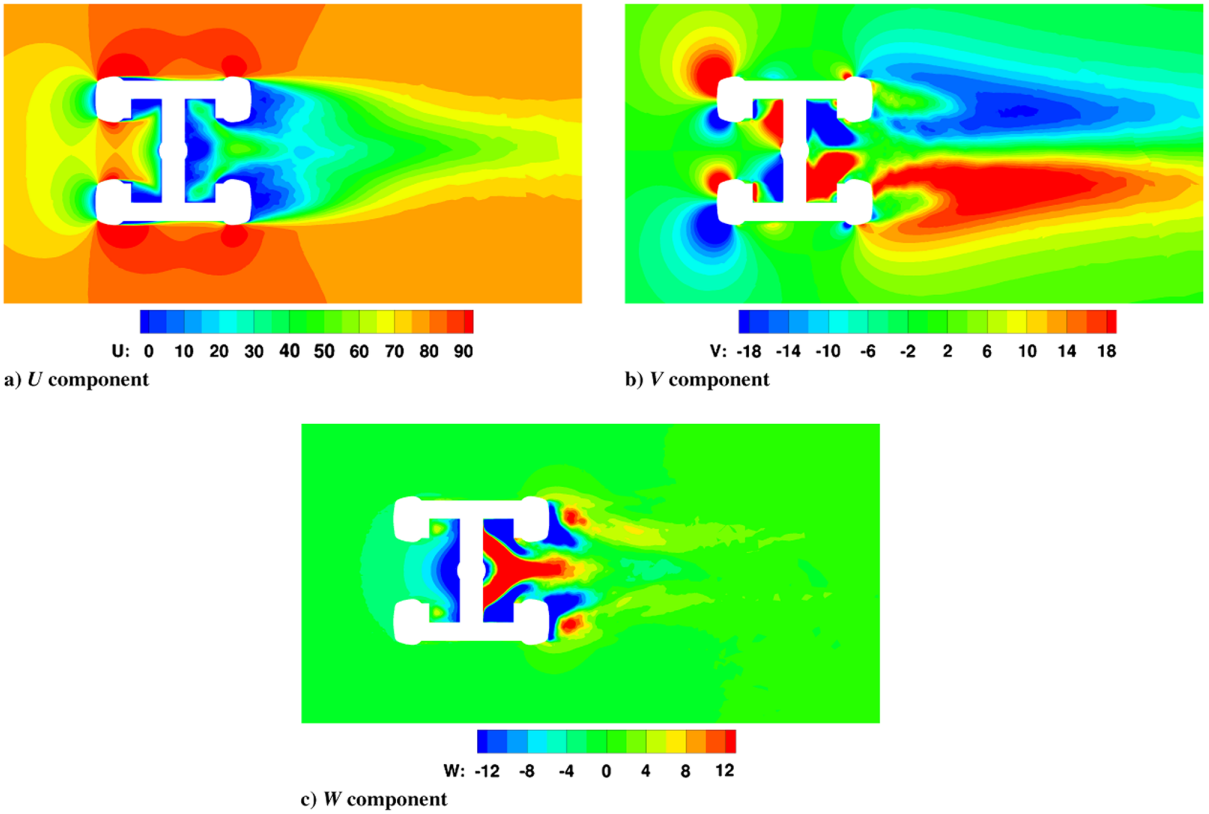

a) *U* component b) *V* component c) *W* component

Fig. 17 Mean velocity contours of the three velocity components for the improved grid.

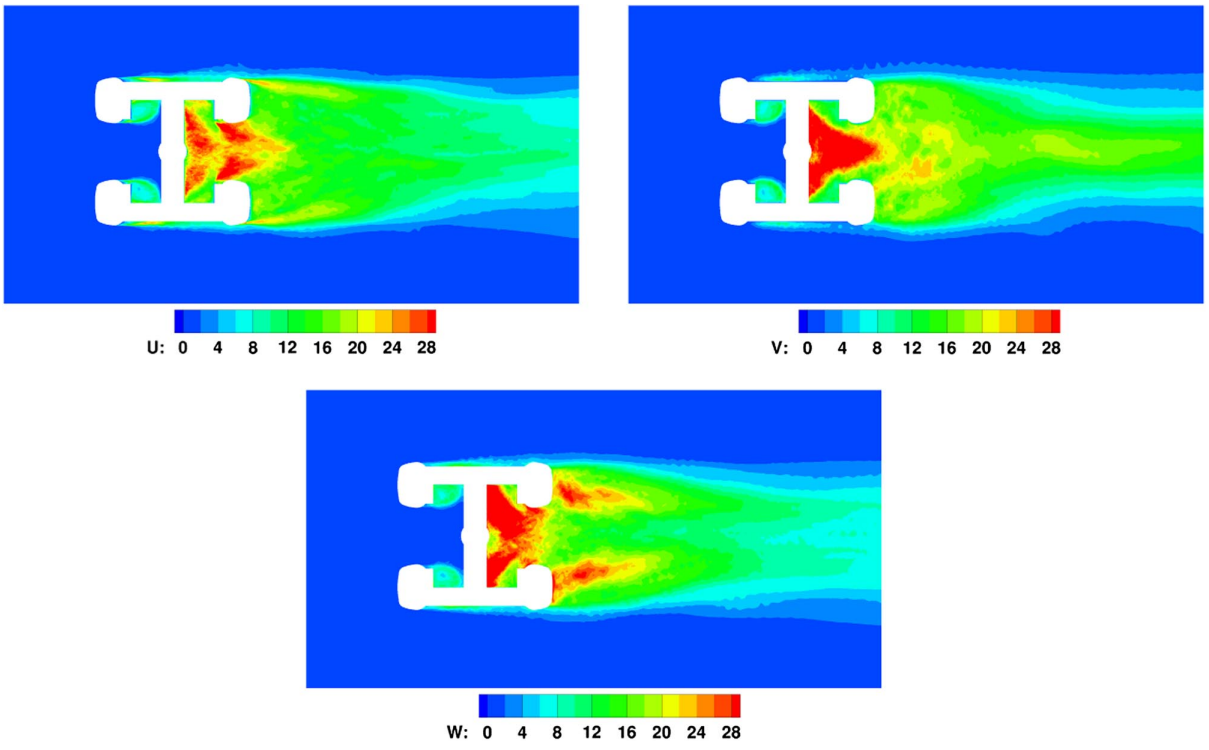

Fig. 18 RMS velocity contours of the three velocity components for the baseline grid.

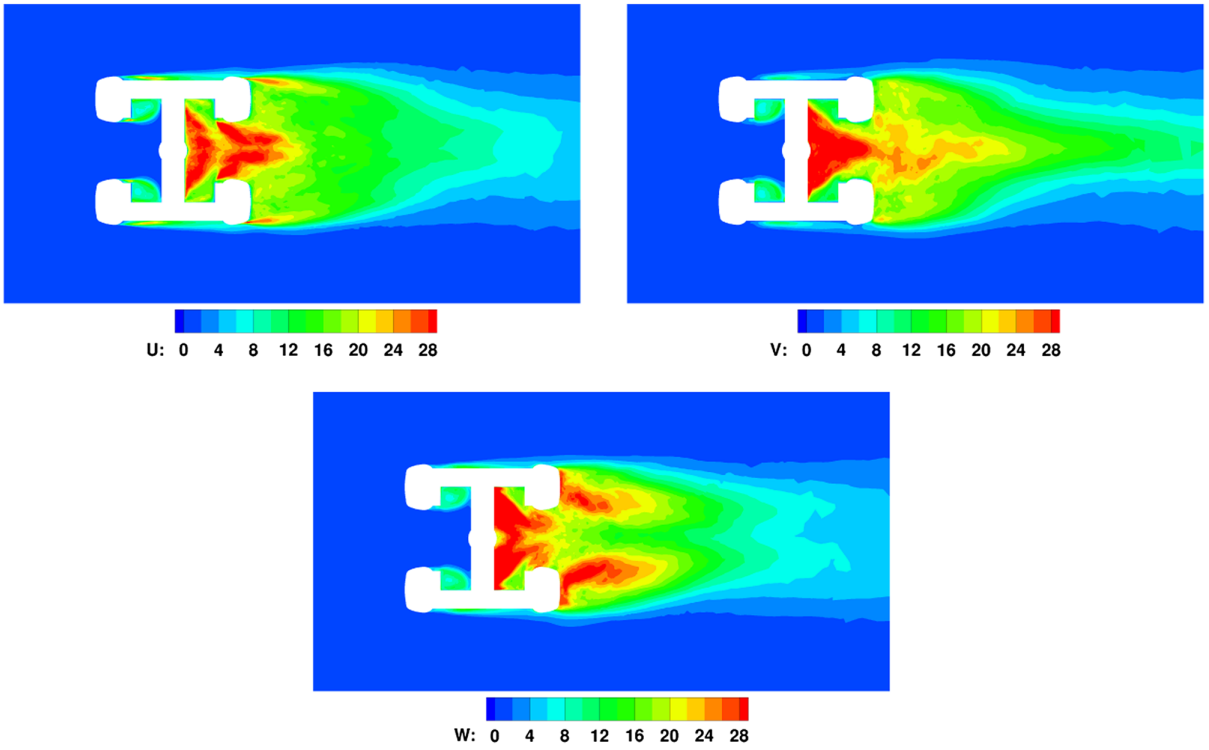

Fig. 19 RMS velocity contours of the three velocity components for the improved grid.

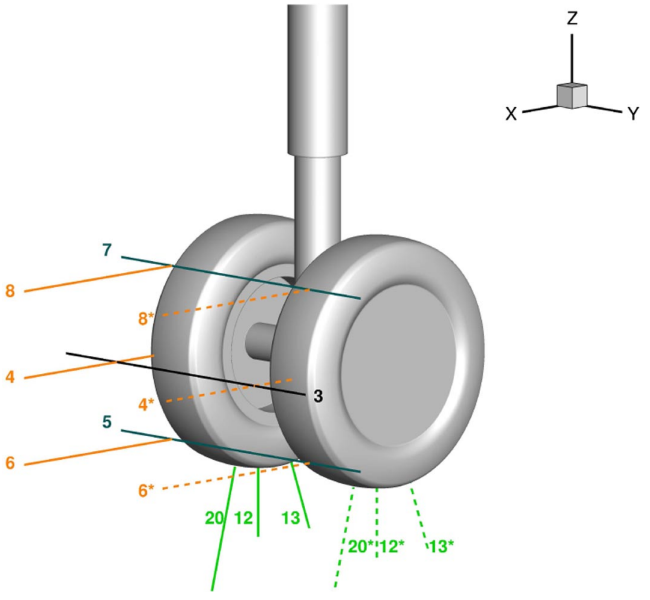

Fig. 20 Measurement lines with LDV2D from experiments.

Velocity profiles along the wake are shown for the same positions (see Fig. 20) of the LAGOON experiment performed by ONERA, in Figs. 21–25. The experiments include mean and rms data generated by both PIV and laser Doppler velocimetry (LDV) techniques in two and three dimensions (LDV2D and LDV3D, respectively). Deviations in velocity magnitude are expected due to the different boundary conditions of the simulation compared to the experiments, in which a closed-wall wind tunnel was used. The confinement may reduce both w and v velocity components while increasing the u component. In the simulation, an open domain is employed, and hence, the fluid adjusts smoothly to the presence of the landing gear.

For comparing the numerical solutions and experimental data from the LDV3D, several lines are used as reference behind the wheels at the $z = 0.0$ m plane. However, in the experiments, only the wake of one of the wheels was measured. Hence, we simply mirror the experimental results using dashed lines in Figs. 21 and 22 as a reference for the numerical computations. Results obtained by the LDV2D, shown in Figs. 23–25, do not include the v component of the velocity in the experiments, and they are computed along the numbered lines in the positions indicated in Fig. 20. Since the landing gear is symmetric with respect to the y axis, results are presented for both $\pm y$ axis coordinates in order to have more data regarding the convergence of flow statistics. The mirrored lines are denoted by $*$ together with the original line number.

In general, numerical results show good agreement with experimental data in terms of mean velocities for both grids. However, for the rms velocity components, the overall agreement is better for the improved mesh, especially closer to the landing gear surface where the mesh is finer (see Figs. 21 and 25, for instance). Away from the solid surface, the rms values for the baselined grid provide a slightly better agreement to the experimental measurements (see Fig. 22).

C. Acoustic Predictions

Simulations presented in the BANC workshop employed both solid and permeable FWH surfaces, where the solid surface coincides with the landing gear surface while the permeable surface surrounds the geometry and portions of the wake. Literature results for the permeable surface show a damping of the high-frequency noise and an increase in the low-frequency content of the spectrum [35]. The positioning of the permeable surface is a very sensitive task, and its postprocessing requires some manipulation of the data to avoid the behavior discussed previously. Also, the influence of the quadrupole sources in the wake is proportional to M^8, and since the freestream Mach number in the current simulation is low ($M_\infty = 0.23$), these sources can be neglected. Furthermore, the results of the solid surfaces in the BANC computations are generally better than those obtained by the porous surfaces for the same case, and hence only the solid surface is employed here.

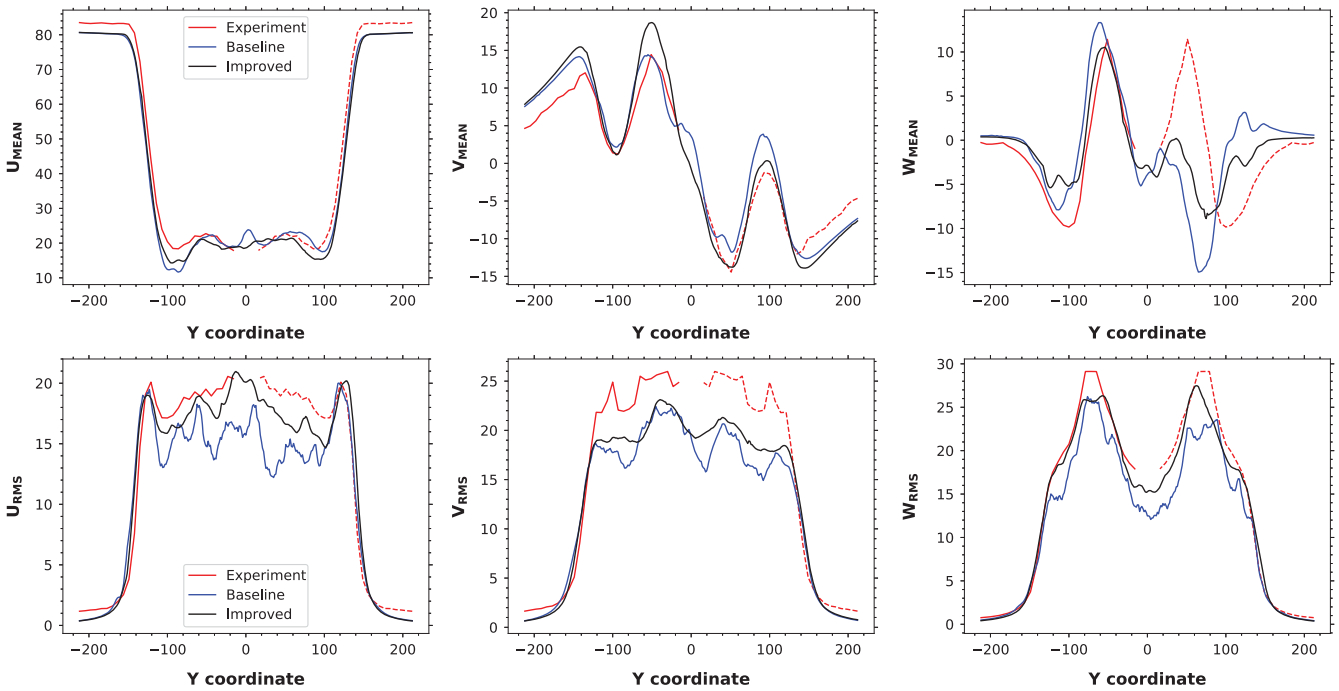

Fig. 21 Velocity profiles from numerical simulations and experimental data from LDV3D at $x = 234$ mm.

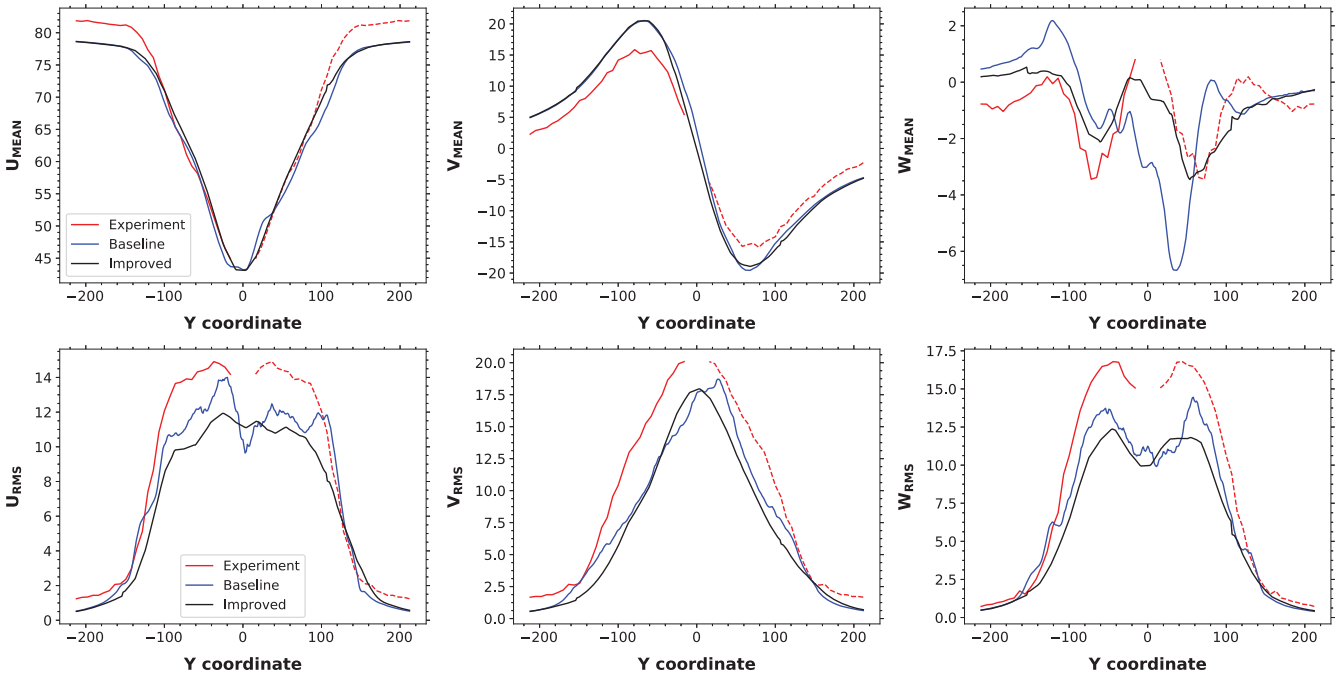

Fig. 22 Velocity profiles from numerical simulations and experimental data from LDV3D at $x = 460$ mm.

The current acoustic predictions are compared to the experimental results presented in [23]. In this reference, the microphones are positioned as shown by the sketch from Fig. 26. To compare the current numerical predictions to the experimental data, accounting for shear layer refraction effects on sound propagation would be required. Hence, we evaluate the far-field noise in terms of the pressure PSD for modified microphone positions as discussed by [15].

In the sound prediction of a landing gear in-flight condition, the effect of the freestream should be included on the propagation of acoustic waves to the observers. However, in the anechoic wind tunnel in which the experiments are conducted, the effects of the freestream velocity only occur around the landing gear surface, and the microphones are positioned away from the jet axis as shown in the sketch of Fig. 26. Therefore, a considerable portion of the acoustic radiation occurs in a quiescent medium, and an evaluation of the far-field noise considering freestream conditions for the whole path of the propagation of acoustic waves may not be consistent with the experiments. Therefore, results of the far-field noise prediction are evaluated for two situations. The first considers the influence of the

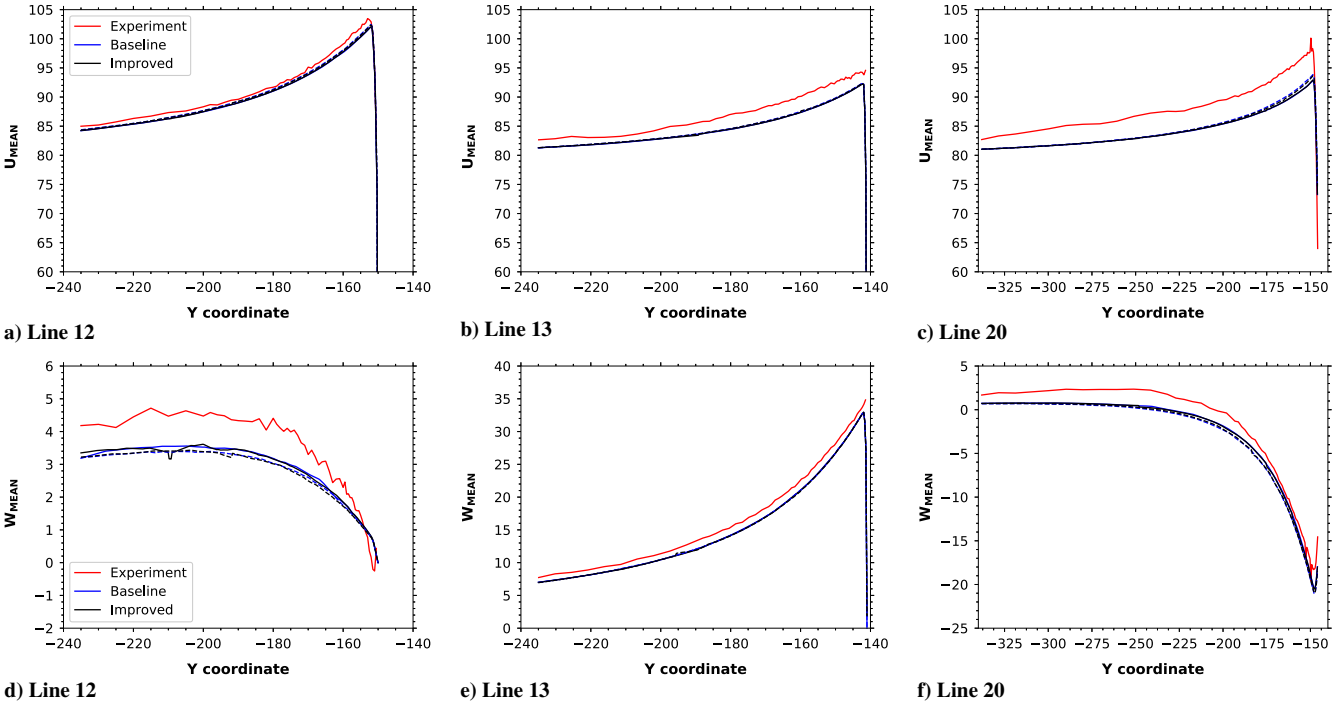

Fig. 23 Boundary layer velocity profiles for different probes measured along the vertical distance z to the wheel surface.

freestream velocity in the FWH analogy, and the second assumes a quiescent condition in the propagation. In this latter case, one should remember that the acoustic sources computed from the numerical simulations already account for the nonuniform flow effects along the landing gear.

Acoustic predictions are only presented for the second simulation with the improved grid since, for this case, the statistics are better converged. Results of the FWH acoustic analogy are shown in Figs. 27 and 28 for three different microphone positions in flyover and sideline configurations, respectively. To check for any asymmetry in the noise prediction, sideline microphones are placed at both sides of the landing gear (black and gray curves in the plots).

The dipole sources at the surface are computed using 19 windows containing 2048 snapshots and an overlap of 50% together with the Tukey window function with the control parameter set as 0.25. It is possible to see that results are very similar when the right and left sideline microphones are compared. Regarding the FWH acoustic analogy for propagation of sound waves, it is possible to see that a better match of the spectra is obtained when the quiescent medium is considered in the propagation to the observer positions. For the sideline positions, it is possible to notice the tonal components at 1 and 1.5 kHz previously observed in the surface pressure spectra. These tones are also present in the experimental measurements; however, for some microphones, they are overpredicted in the numerical simulation, as shown in Figs. 28a and 28f.

Overall, the PSD of the far-field pressure shows better agreement with the experimental data than that of surface pressure. One should remember that, while the PSD for the surface pressure represents the values of pressure fluctuations at one specific point in the landing gear surface, the far-field noise is computed as the integral of the pressure fluctuations along the entire surface. In general, the surface pressure fluctuations are poorly captured in regions where the flow is quasi-steady or when the mesh is less refined. The regions where pressure fluctuations are more intense, for example, those where flow separation occurs, have a finer mesh and show better agreement with experiments. These regions are more relevant to the acoustic prediction and are better resolved by the simulations.

Since the pressure fluctuations on the cavity are intermittent, it is expected that the noise from the dipole sources along its surface should change according to the window for which they are computed, as shown in Fig. 29. According to the results of the wavelet transform in Fig. 14, the pressure fluctuations should be maximum for the sample bin in which a strong peak is observed. Since the magnitudes of the noise sources are different for the individual bins, the acoustic measurements in the far field are also different. This is shown by a directivity plot of acoustic pressure at 1.5 kHz in the plane $z = 0.0$ m shown in Fig. 30. This figure shows the directivities computed for the individual bins from Fig. 29. One can see in this figure that the far-field pressure amplitudes are strongly varying in time while the overall pattern of the noise radiation is similar.

D. Proper Orthogonal Decomposition

Proper orthogonal decomposition was first applied in the context of fluid mechanics by Lumley [36] to extract coherent structures in turbulent flows. This method is based on the principal component analysis (PCA), a statistical procedure that employs orthogonal transformation to convert a set of Nt observations of correlated variables measured at a time instant t at Ng locations $\boldsymbol{x}$ into a set of linearly uncorrelated variables called principal components or modes, ϕ. Each mode has an associated amplitude coefficient, given by the matrix A. By construction, these modes have minimum variance, which makes PCA/POD optimal in terms of reconstruction of the original data if one uses only a few modes. It is possible to make the inverse transformation according to

$$U(\boldsymbol{x}, t) = \Phi_i(\boldsymbol{x})A(t)^T \tag{1}$$

where A is a unitary square matrix with size Nt and Φ is a rectangular matrix with shape $Ng \times Nt$.

To keep this task computationally tractable, one should concatenate the solution at each time step in the form of a column vector of a matrix. This creates the matrix with all observations. Then, one should compute the correlation matrix of the data using either a temporal or spatial correlation, depending on the size of the measured data. If there are more columns than rows (more time samples than spatial probe locations), as is generally the case of experiments, one should employ a spatial correlation. In numerical simulations, one should compute the temporal correlation since the number of grid points is usually larger compared to the number of temporal solutions. This latter approach is called the snapshot method, and it

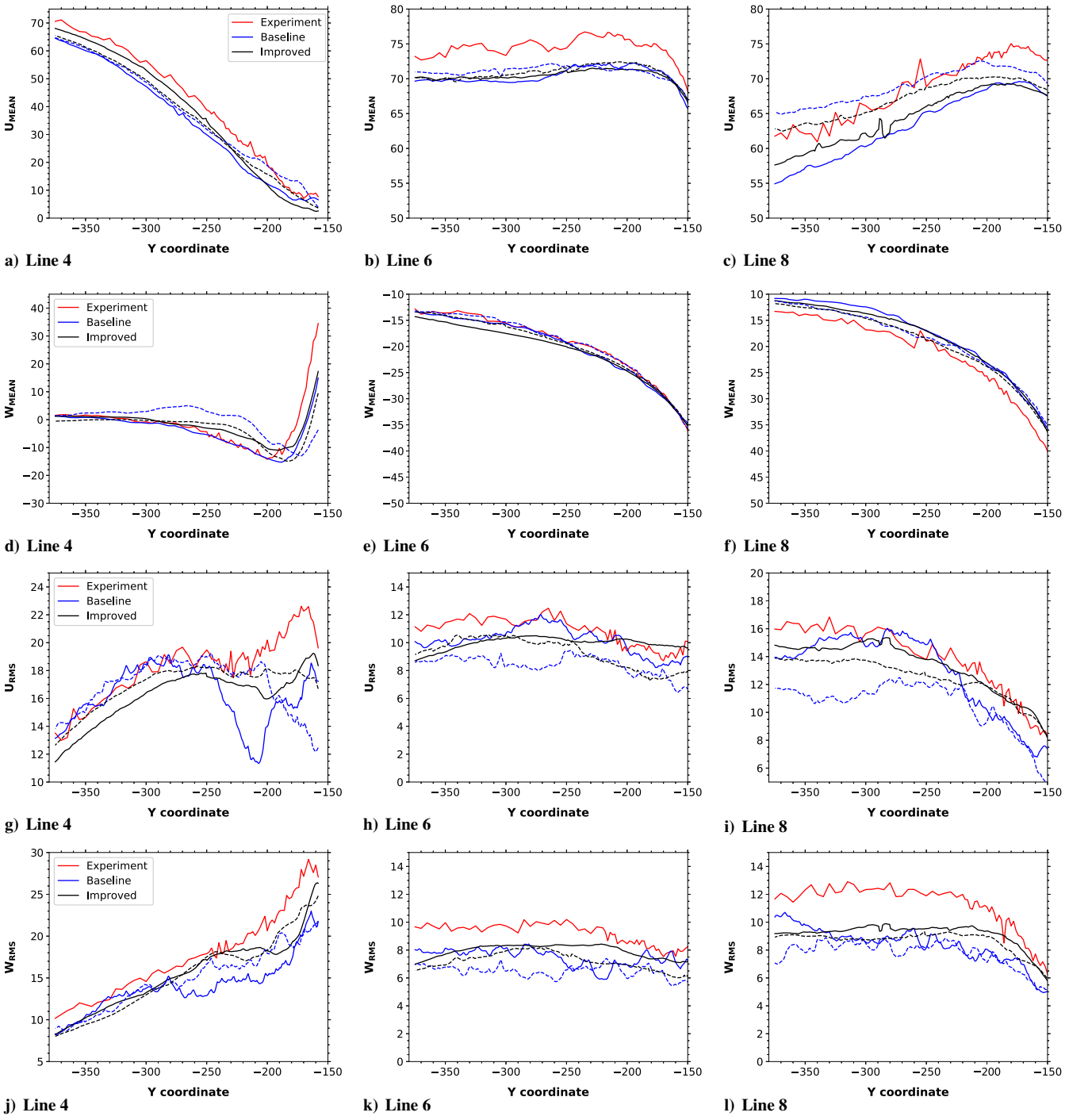

Fig. 24 Velocity profiles for lines shown in Fig. 20.

was proposed by Sirovich [37]. The snapshot method leads to the same results of the classic POD proposed previously by Lumley [36]. For incompressible flows, the data used for the computing the POD correlation matrices are often based on turbulent kinetic energy, which is proven to reduce the error in the energy norm. However, for compressible flows, other norms can be employed since thermodynamic variables play an important role in the total energy of the flow.

In this Paper, we employ the POD in order to identify possible coherent structures responsible for tonal noise generation in the LAGOON landing gear. With the acquisition of flow data from simulation performed using the improved grid, the temporal correlation matrix C is obtained using a kinetic energy norm as

$$C_{ij} = \Sigma_{k=1}^{Ng}[u'(x_k,t_i)u'(x_k,t_j) + v'(x_k,t_i)v'(x_k,t_j) + w'(x_k,t_i)w'(x_k,t_j)]V_k \quad (2)$$

Here, we have i and $j \leq Nt$, with Nt and Ng being the number of snapshots and grid points, respectively. Finally, the singular value decomposition (SVD) of the correlation matrix leads to the singular values λ, which order the modes by their energy content. Furthermore, the left singular matrix A gives the temporal dynamics of each mode, i.e., the coefficients $a(t)$ of the matrix A, computed from

$$CA = \lambda A \quad (3)$$

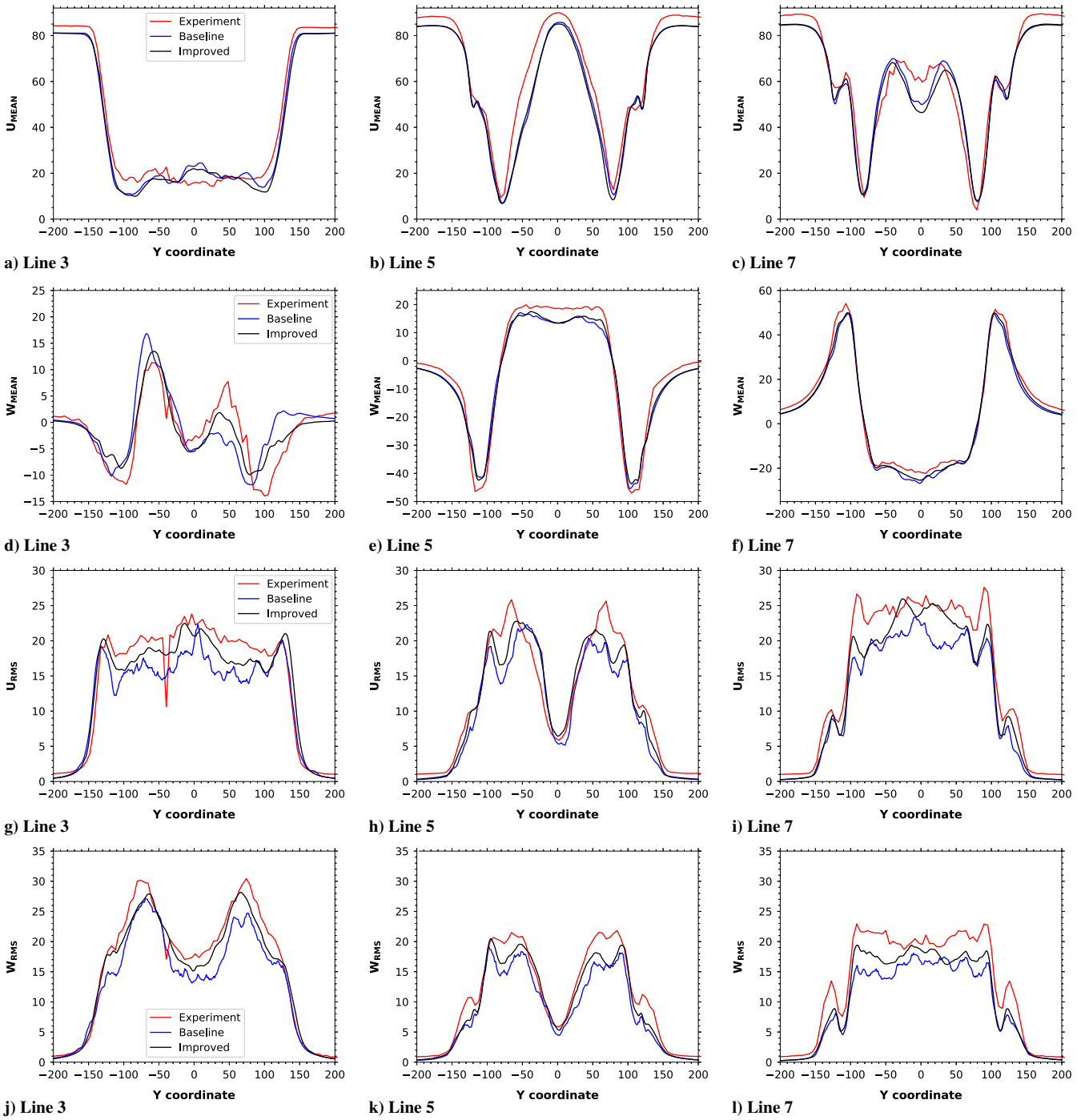

Fig. 25 Velocity profiles for lines shown in Fig. 20.

From this point, the computation of the spatial coefficients is straightforward from

$$\Phi(\boldsymbol{x}) = U(\boldsymbol{x}, t)A(t) \tag{4}$$

To improve the visualization of coherent structures, the spectral POD recently proposed by Sieber et al. [24] is used in this work. The main idea of this method is to filter only the correlation matrix C, such that it acts as a spectral filter of the temporal modes A of the standard snapshot POD. The outcome from the SVD of the filtered matrix leads to a preferential band of frequencies in each mode, resulting in "cleaner" spatial modes. The parameters of the spectral proper orthogonal decomposition (SPOD) are related to the filter shape or by its half-width Nf, such that its entire width is given by $2Nf + 1$. This parameter cannot be wider than the size of the matrix Nt. Unfortunately, the choice of the parameters in the filtering process of the SPOD is not straightforward, and some trial and error is required to achieve the desired results. For example, if one employs a boxcar filter with width equal to the entire size of the matrix and also assumes that the nonfiltered correlation matrix is circulant, the result is a Toeplitz matrix. In this case, the eigenvectors (temporal modes) are pure sinusoids, and hence the spectral POD converges to a discrete Fourier transform. One should keep in mind that this approach is very aggressive, and in order to visualize the dynamic of coherent structures at a frequency band, one should either reduce the filter width or employ a filter with a smoother response in the frequency domain.

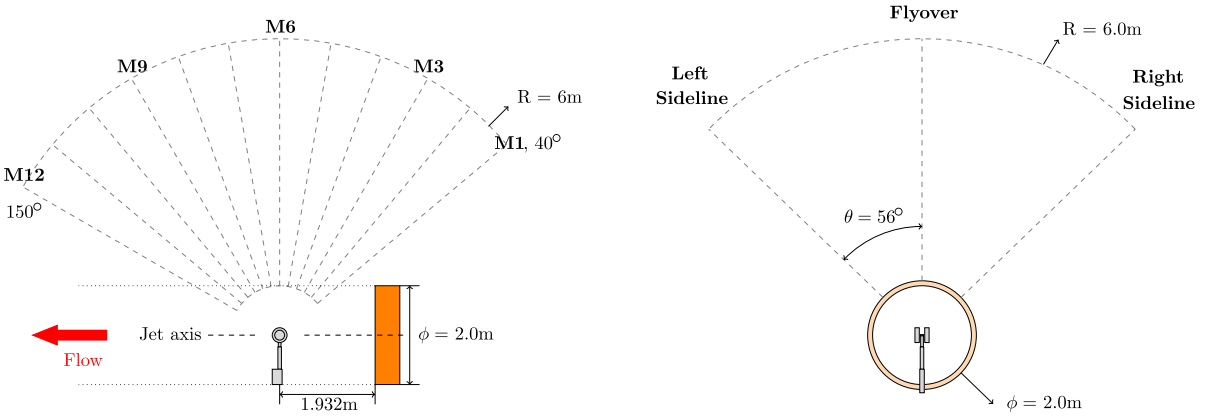

Fig. 26 Microphone positions in the BANC experiments adapted from [8].

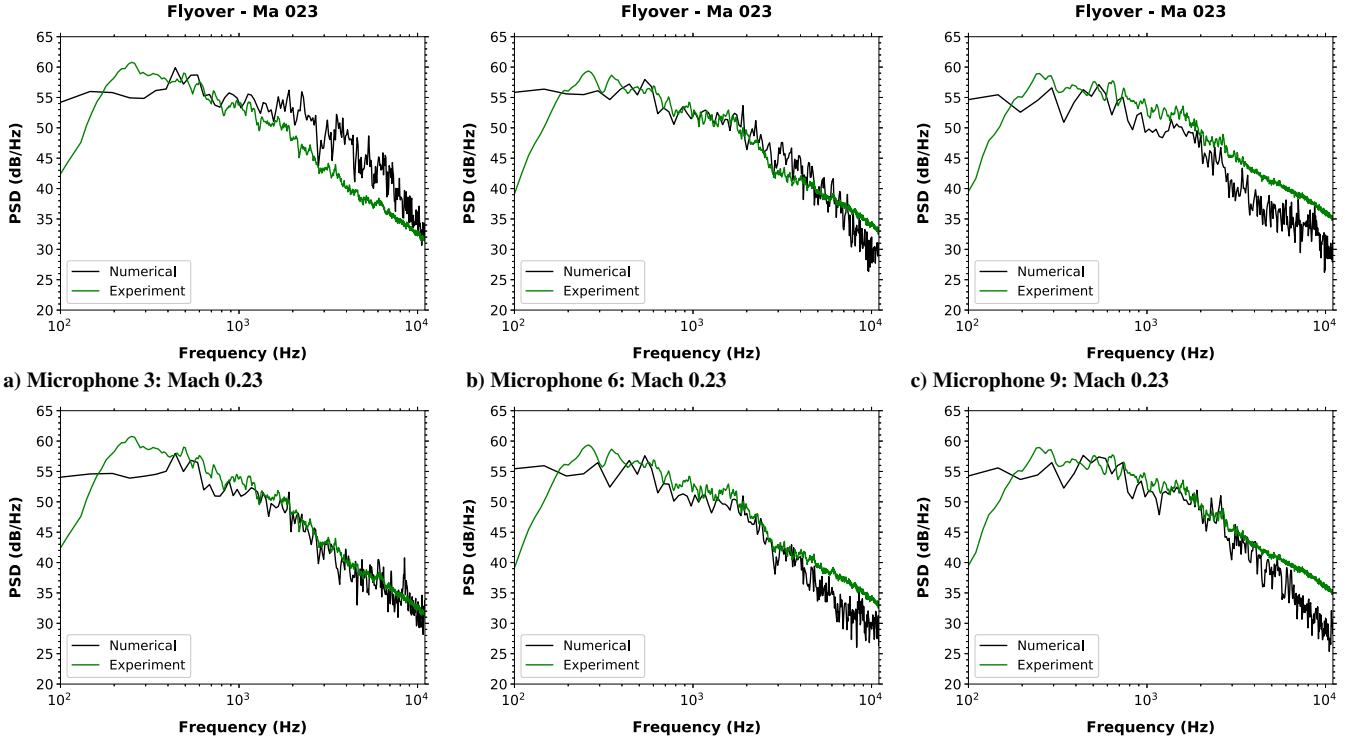

a) Microphone 3: Mach 0.23 **b) Microphone 6: Mach 0.23** **c) Microphone 9: Mach 0.23**

d) Microphone 3: Mach 0.00 **e) Microphone 6: Mach 0.00** **f) Microphone 9: Mach 0.00**

Fig. 27 Power spectral density of far-field noise measured in the flyover microphones.

The main idea in this first assessment of the POD for the LAGOON configuration is to investigate the noise sources in the tonal noise generation by the cavity at 1.5 kHz. Hence, the domain in which the correlation is performed includes only the region around the wheel, i.e., inside a cubic box from −200 to 200 mm. Also, the number of snapshots Nt is 577, and the time increment between each snapshot is 8×10^{-5} s. Two different filters have been studied, a Gaussian filter and a boxcar filter, and their half-width Nf is either null, 144, or 288. Finally, we assume that the correlation matrix is circulant, which is shown to improve the harmonic correlation of the POD modes [38]. Results for different filtering parameters are shown in terms of the filtered correlation matrix in Fig. 31.

Since the main interest is to find turbulent coherent structures responsible for the tonal noise, a Fourier transform of the temporal modes is required to identify structures excited at 1.5 kHz. After an assessment of the full spectrum of POD modes, we observe that mode 129 or 127 is associated to the target frequency if a boxcar or Gaussian filter, respectively, is employed. Results are shown in Fig. 32a for the boxcar filter. This approach concentrates all the energy in a single frequency when the filter width has the size of the entire matrix. One should remember that the windowing in the Fourier transform may cause spectral leakage. On the other hand, results for the Gaussian filter are shown in Fig. 32b, and one can see that this approach allows a wider response in the frequency domain compared to the boxcar filter due to the response properties of the filters. Therefore, it is possible to obtain the energetic content of a specific mode for a narrow band of frequencies.

With the computation of the temporal modes, it is possible to obtain the associated spatial eigenfunctions based on Eq. (4). Results using the snapshot method are shown in Fig. 33a in terms of isosurfaces of v velocity fluctuations for the POD mode 129, which is indicated by the blue line in Fig. 32a. In this figure, the structures are not very well defined due to the broadband content. In Fig. 33b, one can see results in terms of isosurfaces of v velocity fluctuations using

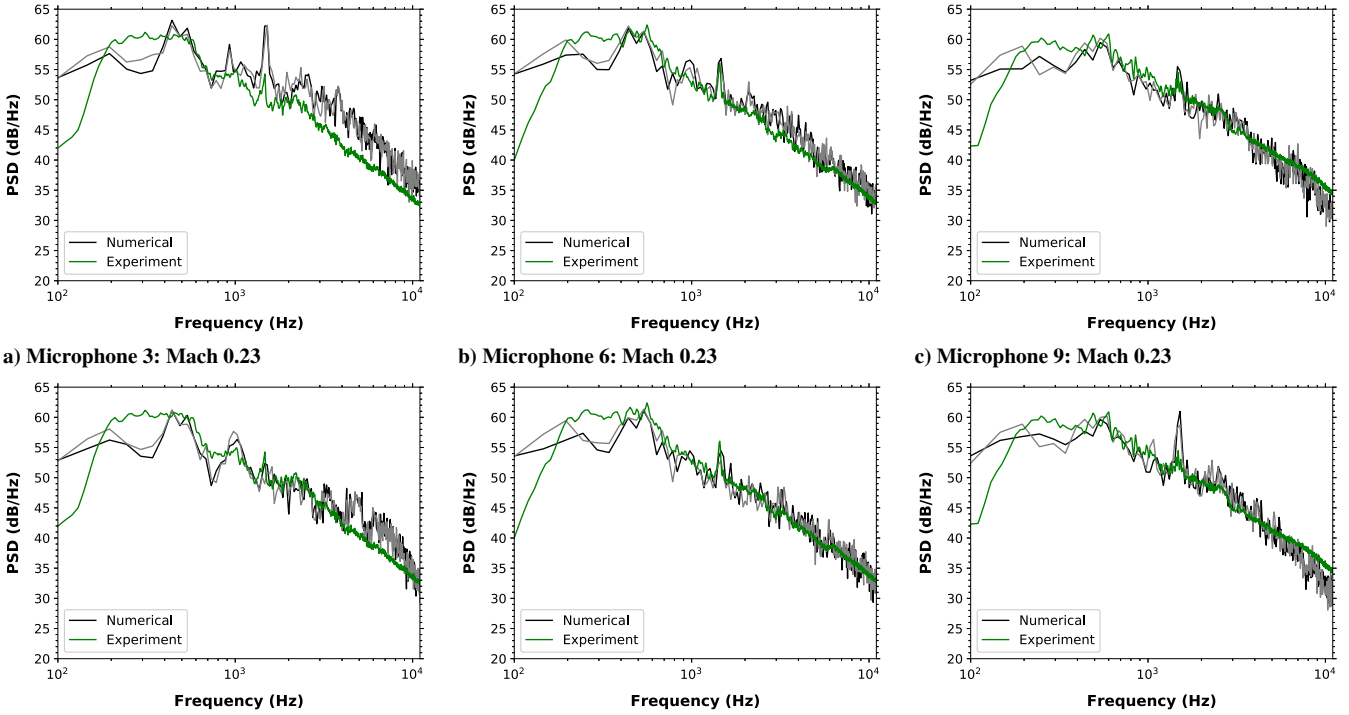

a) Microphone 3: Mach 0.23 b) Microphone 6: Mach 0.23 c) Microphone 9: Mach 0.23

d) Microphone 3: Mach 0.00 e) Microphone 6: Mach 0.00 f) Microphone 9: Mach 0.00

Fig. 28 Power spectral density of far-field noise measured in the sideline microphones.

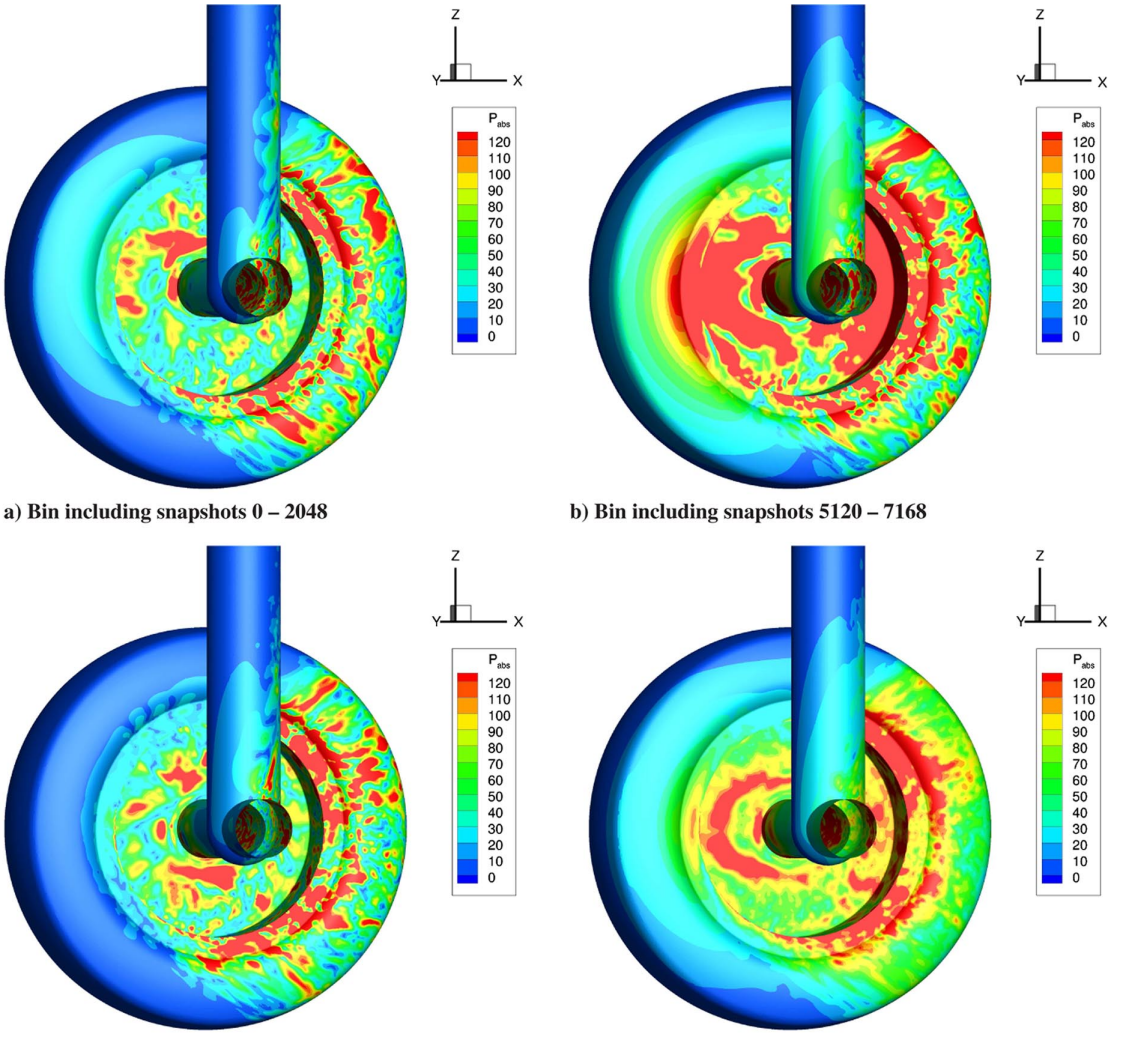

a) Bin including snapshots 0 – 2048 b) Bin including snapshots 5120 – 7168

c) Bin including snapshots 8192 – 10240 d) Average of bins from Figs. 29 a – c

Fig. 29 Pressure fluctuations along the cavity region for 1.5 kHz.

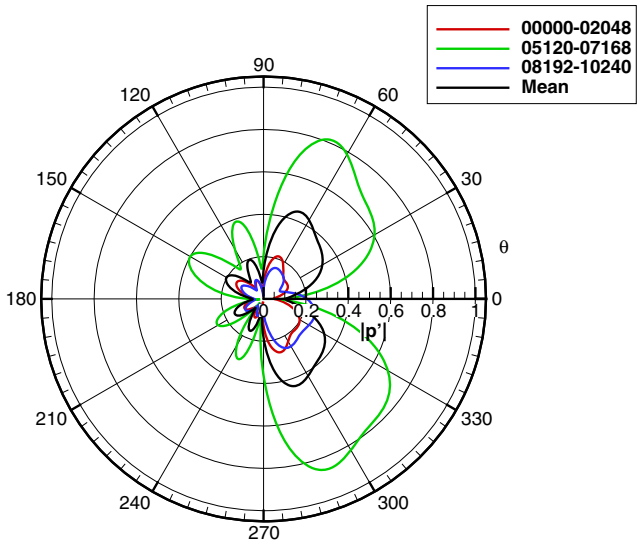

Fig. 30 Pressure directivity plot in the plane $z = 0.0$ m for different bins and frequency 1.5 kHz.

the spectral POD obtained from the orange curve from Fig. 32. With the filtering of the correlation matrix, it is possible to identify quasi-two-dimensional coherent turbulent structures with a dominant frequency around 1.5 kHz generated at the edge of the cavity. Since this frequency is associated with the resonance modes of the cavity, these structures are likely to be the noise sources exciting such tones [17,18]. Since two-dimensional structures are very efficient noise sources, any device that breaks this coherence could lead to a reduction of the tonal noise.

Contour plots at different planes normal to the z axis show that the presence of the strut and axle changes the pattern of the coherent structures on the upper portion of the cavity. In Fig. 34a, one can see that the coherent structures are transported along the cavity, possibly reaching the cavity downstream edge. This could lead to the excitation of Rossiter modes in the cavity. Figure 34b shows that the axle affects the advection of the coherent structures that impinge on the junction between the bottom of the cavity and the axle, preventing the structures from hitting the downstream edge. Finally, Fig. 34c shows that the local acceleration due to the presence of the axle and strut changes the dynamics of the structures, reducing their spatial correlation for this particular POD mode.

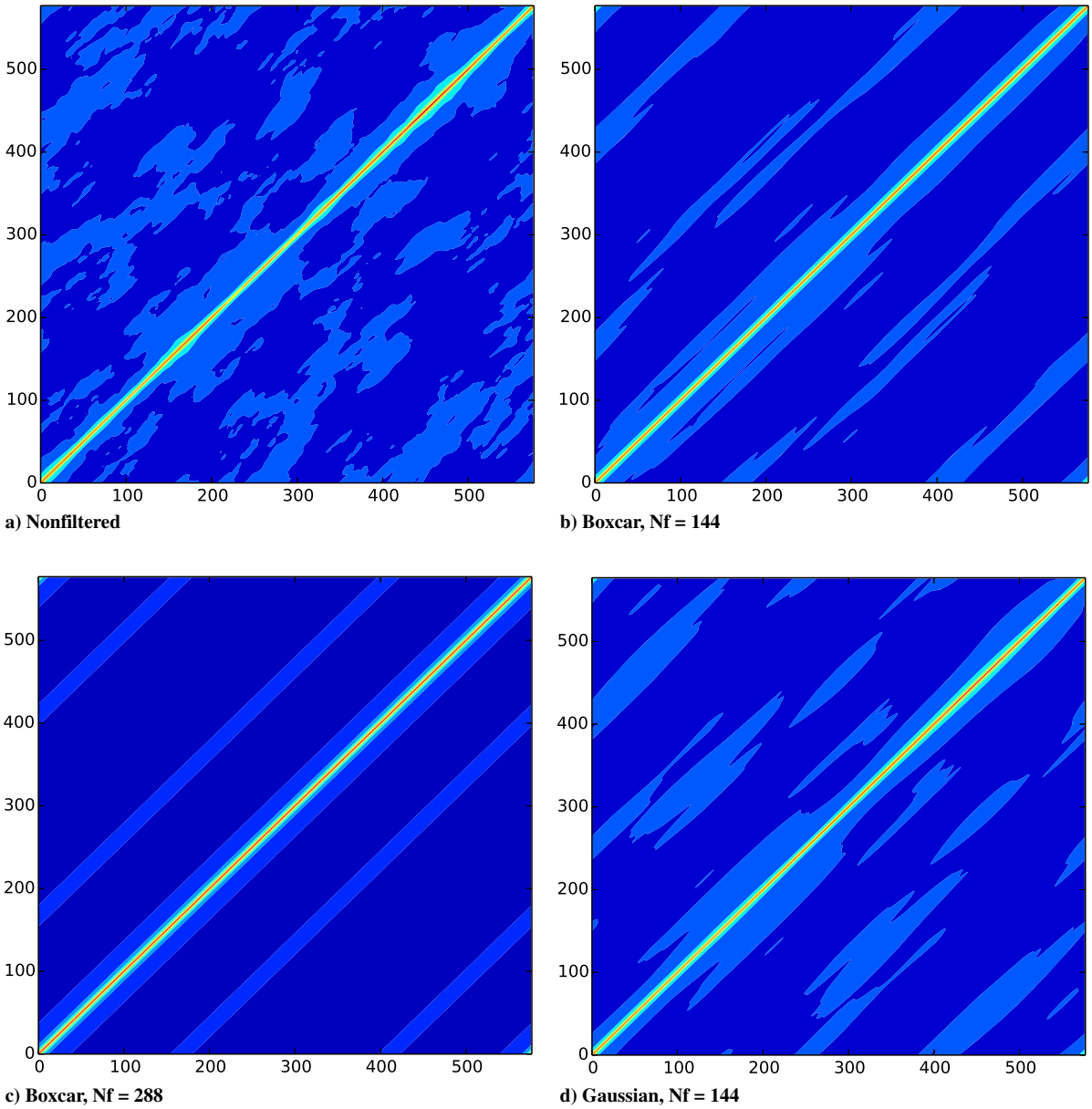

a) Nonfiltered **b) Boxcar, Nf = 144**

c) Boxcar, Nf = 288 **d) Gaussian, Nf = 144**

Fig. 31 Correlation matrix obtained using different filter parameters.

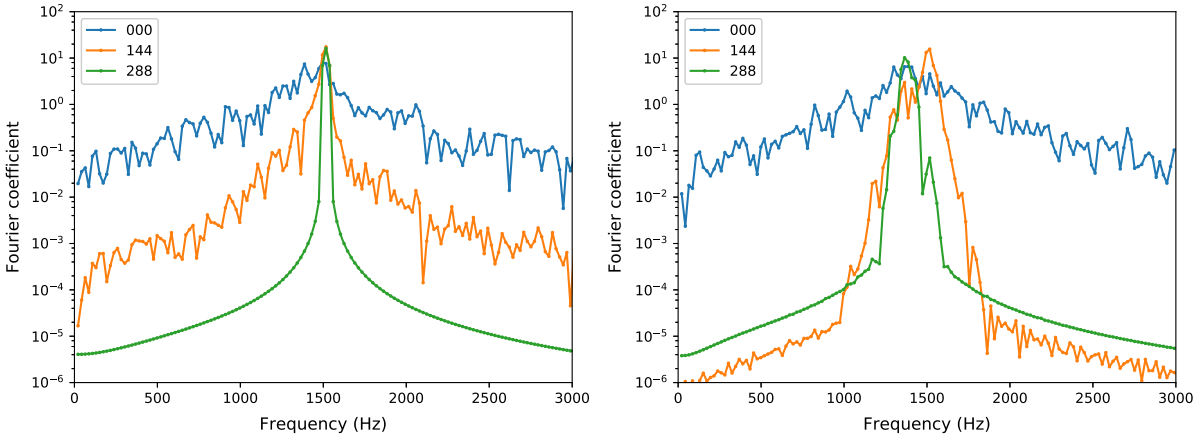

a) Boxcar filter (mode 129) b) Gaussian filter (mode 127)

Fig. 32 Spectral content of temporal modes in the POD of the LAGOON.

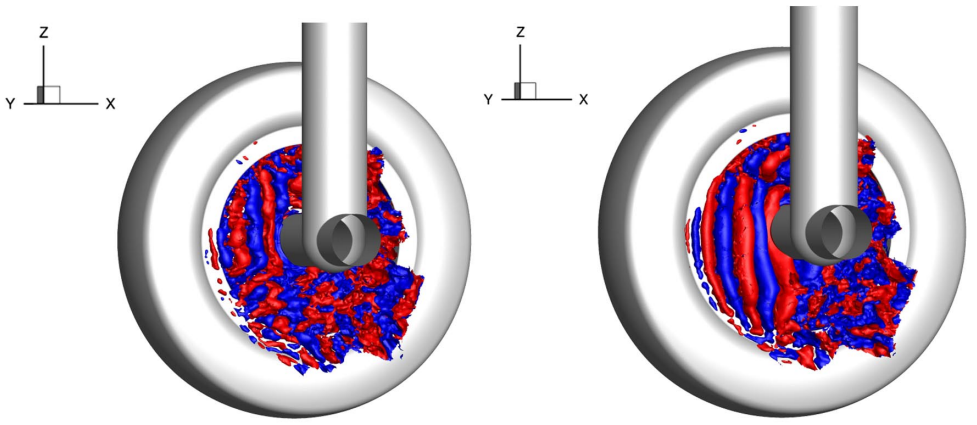

a) Snapshot POD b) Spectral POD

Fig. 33 Isosurfaces of v velocity fluctuations inside the LAGOON cavity.

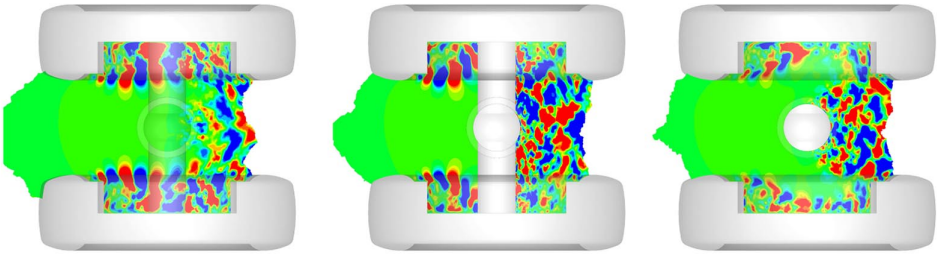

a) Cut at $z = -33$ mm b) Cut at $z = 0$ mm c) Cut at $z = +33$ mm

Fig. 34 Contour plots of v velocity fluctuations inside the cavity for 1.5 kHz.

IV. Conclusions

The current work presents numerical simulations of the AIRBUS–ONERA LAGOON landing gear configuration. Detached-eddy simulations are performed, and results are shown in terms of mean and rms values for pressure on the landing gear surface, velocity profiles along the wake and boundary layers, and also far-field noise predictions computed by the FWH acoustic analogy. Comparisons to experimental data show good agreement, validating the present methodology.

A first grid (called the baseline here) is designed based on literature results of the current landing gear geometry. In this sense, grid refinement is employed along critical regions of the flow, e.g., the axle and the cavity. Other flow regions that should have a minor contribution to the noise generation mechanisms are coarsened to reduce simulation costs. With the knowledge acquired from the initial assessment of the baseline simulation, a new grid called *improved* here is designed to achieve enhanced results. To do so, the surface mesh is more isotropic, leading to a reduced numerical dissipation and a better prediction of the unsteady near-field data. Using the new mesh, the total temporal signal of the simulation is also increased to achieve a better statistical convergence of the turbulent quantities and acoustic data.

With the new mesh, improved results can be observed in terms of pressure fluctuations on the landing gear surface when compared to Kulite data from experiments. Moreover, this Paper also observes a better match with experiments in terms of the velocity field along the

wake since the improved grid is refined closer to the geometry. This is highlighted by the results in terms of the velocity component w, in which more symmetric profiles in terms of mean values can be observed. Higher rms values close to the body are obtained by the improved mesh due to the reduced numerical dissipation. Finally, the coarsening of portions of the wake far from the body does not seem to compromise the results.

Aeroacoustic predictions are performed using the FWH acoustic analogy considering uniform flow effects in the acoustic propagation. In the present simulations, the freestream Mach number is set as 0.23, and the acoustic predictions are computed for this particular case. However, since the experiment is performed in an anechoic chamber, the computation of the far-field noise is also performed by considering the propagation medium to be quiescent. For this case, one could observe that better comparisons to experiments are achieved in terms of noise predictions.

An analysis of the pressure fluctuations in the cavity shows that the tonal noise at 1.5 kHz is intermittent. In this context, a wavelet transform is employed to show that strong pressure fluctuations occur at specific bins of the dataset. This analysis demonstrates that the magnitudes of the surface pressure sources are strongly varying in time and hence lead to different amplitudes of the far-field noise. However, this intermittency does not change the overall pattern of the noise radiation.

The use of proper orthogonal decomposition allows the identification of coherent two-dimensional structures in the upstream region of the cavity, along the shear layer. A comparison between the snapshot method and the spectral POD shows that the latter is able to increase correlation of the spectral content with fewer POD modes. This leads to a more defined visualization of the spatial modes and a better identification of coherent structures at specific frequencies. The objective of the current POD and wavelet analysis of the LAGOON landing gear is to identify patterns in the flow that may be associated to frequencies around 1.5 kHz and that excite cavity resonances. In this context, the presence of the strut and axle changes the pattern of the coherent structures on the upper portion of the cavity. This Paper also observes that, under the axle, coherent structures may reach the downstream edge of the cavity, possibly exciting Rossiter modes. In the midplane, the turbulent structures impinge on the junction between the bottom of the cavity and the axle.

Acknowledgments

The authors gratefully acknowledge the partial support for this research provided by Conselho Nacional de Desenvolvimento Científico e Tecnológico under research grant number 305277/2015-4. This work is also supported by Fundação de Amparo à Pesquisa do Estado de São Paulo under research grants numbers 2013/03413-4 and 2013/07375-0. The computational resources provided by Centro Nacional de Processamento de Alto Desempenho are also gratefully acknowledged through project 551. The Boeing Company is acknowledged for supporting the present research project through project number 2013-8985 and also for sharing the BCFD code used in the numerical simulations. We acknowledge Andrew Cary, Deric Babcock, Mark Fisher, and Nicholas Moffitt for several fruitful discussions about technical details of this work. We finally would like to thank José Fregnani and Antonini Macedo, from Boeing Research & Technology Brazil (BR&TB), and Paul Bent, from Boeing Research & Technology (BR&T), for supporting the current research project. We acknowledge Eric Manoha for providing the experimental data used for comparison in the current work. The LAGOON database is owned by ONERA and Airbus Industries, and it was provided to the authors by ONERA under permission by Airbus Industries in the framework of the AIAA BANC Workshop.

References

[1] Dobrzynski, W., "Almost 40 Years of Airframe Noise Research: What Did We Achieve?" *Journal of Aircraft*, Vol. 47, No. 2, 2010, pp. 353–367. doi:10.2514/1.44457

[2] Guo, Y., "A Statistical Model for Landing Gear Noise Prediction," *9th AIAA/CEAS Aeroacoustics Conference*, AIAA Paper 2003-3227, 2003. doi:10.2514/6.2003-3227

[3] Guo, Y., Yamamoto, K., and Stoker, R., "An Empirical Model for Landing Gear Noise Prediction," *10th AIAA/CEAS Aeroacoustics Conference*, AIAA Paper 2004-2888, 2004. doi:10.2514/6.2004-2888

[4] Bennett, G. J., Stephens, D. B., and Verdugo, F. R., "Resonant Mode Characterisation of a Cylindrical Helmholtz Cavity Excited by a Shear Layer," *Journal of the Acoustical Society of America*, Vol. 141, No. 1, 2017, pp. 7–18. doi:10.1121/1.4973212

[5] Oerlemans, S., and Pott-Pollenske, M., "An Experimental Study of Gear Wake/Flap Interaction Noise," *10th AIAA/CEAS Aeroacoustics Conference*, AIAA Paper 2004-2886, 2004. doi:10.2514/6.2004-2886

[6] Khorrami, M., Lockard, D., Humphreys, W., Choudhari, M., and Ven, T. V., "Preliminary Analysis of Acoustic Measurements from the NASA-Gulfstream Airframe Noise Flight Test," *14th AIAA/CEAS Aeroacoustics Conference*, AIAA Paper 2008-2814, 2008. doi:10.2514/6.2008-2814

[7] Guo, Y., "A Study on Local Flow Variations for Landing Gear Noise Research," *14th AIAA/CEAS Aeroacoustics Conference*, AIAA Paper 2008-2915, 2008. doi:10.2514/6.2008-2915

[8] Sanders, L., Manoha, E., Khelil, S. B., and Francois, C., "LAGOON: CFD/CAA Coupling for Landing Gear Noise and Comparison with Experimental Database," *17th AIAA/CEAS Aeroacoustics Conference*, AIAA Paper 2011-2822, 2011. doi:10.2514/6.2011-2822

[9] Sanders, L., Manoha, E., Khelil, S. B., and Francois, C., "LAGOON: New Mach Landing Gear Noise Computation and Further Analysis of the CAA Process," *18th AIAA/CEAS Aeroacoustics Conference*, AIAA Paper 2012-2281, 2012. doi:10.2514/6.2012-2281

[10] Sanders, L., Manoha, E., Khelil, S. B., and François, C., "CFD/CAA Coupling on the LAGOON #2 Landing Gear Using a Structured Multi-Block Solver with the Chimera Technique," *19th AIAA/CEAS Aeroacoustics Conference*, AIAA Paper 2013-2257, 2013. doi:10.2514/6.2013-2257

[11] Giret, J. C., Sengissen, A., Moreau, S., and Jouhaud, J. C., "Prediction of LAGOON Landing-Gear Noise Using an Unstructured LES Solver," *19th AIAA/CEAS Aeroacoustics Conference*, AIAA Paper 2013-2113, 2013. doi:10.2514/6.2013-2113

[12] Liu, W., Kim, J. K., Zhang, X., Angland, D., and Caruelle, B., "Landing-Gear Noise Prediction Using High-Order Finite Difference Schemes," *Journal of Sound and Vibration*, Vol. 332, No. 14, 2013, pp. 3517–3534. doi:10.1016/j.jsv.2013.01.035

[13] Casalino, D., Ribeiro, A. F. P. R., Fares, E., and Nolting, S., "Lattice–Boltzmann Aeroacoustic Analysis of the LAGOON Landing-Gear Configuration," *AIAA Journal*, Vol. 52, No. 6, 2014, pp. 1232–1248. doi:10.2514/1.J052365

[14] Puente, F. D. L., Sanders, L., and Vuillot, F., "On LAGOON Nose Landing Gear CFD/CAA Computation over Unstructured Mesh Using a ZDES Approach," *20th AIAA/CEAS Aeroacoustics Conference*, AIAA Paper 2014-2763, 2014. doi:10.2514/6.2014-2763

[15] Manoha, E., and Caruelle, B., "Summary of the LAGOON Solutions from the Benchmark Problems for Airframe Noise Computations-III Workshop," *21st AIAA/CEAS Aeroacoustics Conference*, AIAA Paper 2015-2846, 2015. doi:10.2514/6.2015-2846

[16] Bulté, J., and Redonnet, S., "Landing Gear Noise Identification Using Phased Array with Experimental and Computational Data," *AIAA Journal*, Vol. 55, No. 11, 2017, pp. 3839–3850. doi:10.2514/1.J055643

[17] Casalino, D., Ribeiro, A. F. P., and Fares, E., "Facing Rim Cavities Fluctuations Modes," *Journal of Sound and Vibration*, Vol. 333, No. 13, 2014, pp. 2812–2830. doi:10.1016/j.jsv.2014.01.028

[18] Giret, J. C., "Simulations aux Grandes Echelles des Ecoulements Instationnaires Turbulents Autour des Trains D'Atterrissage pour la Prediction du Bruit Aerodynamique," Ph.D. Thesis, Inst. National Polytechnique de Toulouse, Toulouse, France, 2014.

[19] Puente, F. D. L., Sanders, L., Druault, P., and Vuillot, F., "Investigation on Landing Gear Shallow Round Cavity Flow Field and Noise Signature," *22nd AIAA/CEAS Aeroacoustics Conferences*, AIAA Paper 2016-2774, 2016. doi:10.2514/6.2016-2774

[20] Oza, U., Hu, Z., and Zhang, X., "Effect of Cavity Flow on Landing Gear Aerodynamic Loads," *22nd AIAA Computational Fluid Dynamics Conference*, AIAA Paper 2015-2288, 2015. doi:10.2514/6.2015-2288

[21] Williams, J. E. F., and Hawkings, D. L., "Sound Generation by Turbulence and Surfaces in Arbitrary Motion," *Philosophical Transactions of the Royal Society of London, Series A: Mathematical and Physical Sciences*, Vol. 264, No. 1151, 1969, pp. 321–342, http://rsta.royalsocietypublishing.org/content/264/1151/321. doi:10.1098/rsta.1969.0031

[22] Manoha, E., Bultè, J., and Caruelle, B., "LAGOON: An Experimental Database for the Validation of CFD/CAA Methods for Landing Gear Noise Prediction," *14th AIAA/CEAS Aeroacoustics Conference*, AIAA Paper 2008-2816, 2008. doi:10.2514/6.2008-2816

[23] Manoha, E., Bulte, J., Ciobaca, V., and Caruelle, B., "LAGOON: Further Analysis of Aerodynamic Experiments and Early Aeroacoustics Results," *15th AIAA/CEAS Aeroacoustics Conference*, AIAA Paper 2009-3277, 2009. doi:10.2514/6.2009-3277

[24] Sieber, M., Pascherei, C. O., and Oberleithner, K., "Spectral Proper Orthogonal Decomposition," *Journal of Fluid Mechanics*, Vol. 792, April 2016, pp. 798–828. doi:10.1017/jfm.2016.103

[25] Mani, M., Cary, A., and Ramakrishnan, S. V., "A General Purpose Euler and Navier–Stokes Solver for Structured and Unstructured Grids," *Journal of Aircraft*, Vol. 42, No. 4, 2005, pp. 991–997. doi:10.2514/1.8591

[26] Cary, A. W., Dorgan, A., and Mani, M., "Towards Accurate Flow Predictions Using Unstructured Meshes," *19th AIAA Computational Fluid Dynamics*, AIAA Paper 2009-3650, 2009. doi:10.2514/6.2009-3650

[27] Spalart, P. R., Jou, W.-H., Strelets, M., and Allmaras, S., "Comments on the Feasibility of LES for Wings, and on a Hybrid RANS/LES Approach," *Advances in DNS/LES*, Greyden, Columbus, OH, 1997, pp. 137–147.

[28] Spalart, P. R., Deck, S., Shur, M. L., Squires, K. D., Strelets, M. K., and Travin, A., "A New Version of Detached-Eddy Simulation, Resistant to Ambiguous Grid Densities," *Theoretical and Computational Fluid Dynamics*, Vol. 20, No. 3, 2006, pp. 181–195. doi:10.1007/s00162-006-0015-0

[29] Spalart, P., and Allmaras, S., "A One-Equation Turbulence Model for Aerodynamic Flows," *30th Aerospace Sciences Meetings*, AIAA Paper 1992-439, 1992. doi:10.2514/6.1992-439

[30] Vatsa, V., Carpenter, M., and Lockard, D., "Re-Evaluation of an Optimized Second Order Backward Difference (BDF2OPT) Scheme for Unsteady Flow Applications," *48th AIAA Aerospace Sciences Meeting*, AIAA Paper 2010-122, 2010. doi:10.2514/6.2010-122

[31] Winkler, C. J., Dorgan, A., and Mani, M., "A Reduced Dissipation Approach for Unsteady Flows on Unstructured Grids," *50th AIAA Aerospace Sciences Meeting*, AIAA Paper 2012-570, 2012. doi:10.2514/6.2012-570

[32] Barth, T. J., and Jespersen, D. C., "The Design and Application of Upwind Schemes on Unstructured Meshes," *27th Aerospace Sciences Meeting*, AIAA Paper 1989-366, 1989. doi:10.2514/6.1989-366

[33] Marcum, D. L., and Weatherill, N. P., "Unstructured Grid Generation Using Iterative Point Insertion and Local Reconnection," *AIAA Journal*, Vol. 33, No. 9, 1995, pp. 1619–1625. doi:10.2514/3.12701

[34] Farge, M., "Wavelet Transforms and Their Applications to Turbulence," *Annual Review of Fluid Mechanics*, Vol. 24, No. 1, 1992, pp. 395–458. doi:10.1146/annurev.fl.24.010192.002143

[35] Azevedo, P. R. G., Jr., and Wolf, W. R., "Noise Prediction of the LAGOON Landing Gear Using Acoustic Analogy and Proper Orthogonal Decomposition," *22nd AIAA/CEAS Aeroacoustics Conference*, AIAA Paper 2016-2768, 2016, pp. 1–10. doi:10.2514/6.2016-2768

[36] Lumley, J. L., "The Structure of Inhomogeneous Turbulent Flows," *Atmospheric Turbulence and Radio Wave Propagation*, Publishing House Nauka, Moscow, USSR, 1967, pp. 166–178.

[37] Sirovich, L., "Turbulence and the Dynamics of Coherent Structures," *Quarterly of Applied Mathematics*, Vol. 45, No. 3, 1987, pp. 561–571. doi:10.1090/qam/1987-45-03

[38] Ribeiro, J. H. M., and Wolf, W. R., "Identification of Coherent Structures in the Flow Past a NACA0012 Airfoil via Proper Orthogonal Decomposition," *Physics of Fluids*, Vol. 29, No. 8, 2017, Paper 085104. doi:10.1063/1.4997202

C. Bailly
Associate Editor